

CFD-analyse av løpehjul og sugerør i en Francis turbin

Simen Røst Breivik

Master i produktutvikling og produksjon
Oppgaven levert: Juni 2011
Hovedveileder: Ole Gunnar Dahlhaug, EPT

MASTEROPPGAVE

for
Stud.techn.

Simen Breivik
Våren 2011

CFD-analyse av løpehjul og sugerør i en Francis turbin
CFD-analysis of a runner and draft tube in a Francis turbine

Bakgrunn

Norske turbiner opererer på meget varierende last i tider med varierende pris og vannnivå i magasinene. Det er en kjent at man får økte utmattingskrefter når turbinene opererer på fullast eller dellast. Ved dellast er turbinene påvirket av utmattingskrefter fra trykkpulsasjoner som blant annet er initiert av strømmingen i sugerøret. Denne sugerør-strømmingen er påført fra løpehjulet og inneholder flere spesielle fenomener som for eksempel "sugerørsvirvelen" og "vortex breakdown". Det er først og fremst den roterende strømmingen som skaper disse fenomenene og fysikken i dette er ennå ikke fullt ut forstått.

Mål

Gjennomføre CFD-analyse av løpehjul og sugerør i en Francis turbin ved dellast

Oppgaven bearbeides ut fra følgende punkter:

1. Litteratursøk
 - a. Finne relevante publikasjoner der det er gjennomført CFD-analyse av løpehjul og sugerør i Francis turbiner
2. Modell test av Francis turbin fra Tokke Kraftverk:
 - a. Komplette hill-diagram skal tegnes etter testen er gjennomført
 - b. Dellast skal undersøkes nøye og fotografier av "dellast-virvelen" skal settes i sammenheng med Hill-diagrammet.
3. Software kunnskap:
 - a. Gjøre seg kjent med ikke-stasjonær strømming med CFX
4. Lage et CFD-grid av løpehjul og sugerør for Francis turbinen ved Tokke Kraftverk
5. Gjennomføre ikke-stasjonære CFD-analyser ved dellast
6. Sammenligning av bilder fra modelltest og resultater fra CFD-analysen

Senest 14 dager etter utlevering av oppgaven skal kandidaten levere/sendte instituttet en detaljert fremdrift- og eventuelt forsøksplan for oppgaven til evaluering og eventuelt diskusjon med faglig ansvarlig/veiledere. Detaljer ved eventuell utførelse av dataprogrammer skal avtales nærmere i samråd med faglig ansvarlig.

Besvarelsen redigeres mest mulig som en forskningsrapport med et sammendrag både på norsk og engelsk, konklusjon, litteraturliste, innholdsfortegnelse etc. Ved utarbeidelsen av teksten skal kandidaten legge vekt på å gjøre teksten oversiktlig og velskrevet. Med henblikk på lesning av besvarelsen er det viktig at de nødvendige henvisninger for korresponderende steder i tekst, tabeller og figurer anføres på begge steder. Ved bedømmelsen legges det stor vekt på at resultatene er grundig bearbeidet, at de oppstilles tabellarisk og/eller grafisk på en oversiktlig måte, og at de er diskutert utførlig.

Alle benyttede kilder, også muntlige opplysninger, skal oppgis på fullstendig måte. For tidsskrifter og bøker oppgis forfatter, tittel, årgang, sidetall og eventuelt figurnummer.

Det forutsettes at kandidaten tar initiativ til og holder nødvendig kontakt med faglærer og veileder(e). Kandidaten skal rette seg etter de reglementer og retningslinjer som gjelder ved alle (andre) fagmiljøer som kandidaten har kontakt med gjennom sin utførelse av oppgaven, samt etter eventuelle pålegg fra Institutt for energi- og prosesssteknikk.

I henhold til ”Utfyllende regler til studieforskriften for teknologistudiet/sivilingeniørstudiet” ved NTNU § 20, forbeholder instituttet seg retten til å benytte alle resultater og data til undervisnings- og forskningsformål, samt til fremtidige publikasjoner.

Ett -1 komplett eksemplar av originalbesvarelsen av oppgaven skal innleveres til samme adressat som den ble utlevert fra. Det skal medfølge et konsentrert sammendrag på maksimalt én maskinskrevet side med dobbel linjeavstand med forfatternavn og oppgavetittel for evt. referering i tidsskrifter).

Til Instituttet innleveres to - 2 komplette kopier av besvarelsen. Ytterligere kopier til eventuelle medveiledere/oppgavegivere skal avtales med, og eventuelt leveres direkte til de respektive. Til instituttet innleveres også en komplett kopi (inkl. konsentrerte sammendrag) på CD-ROM i Word-format eller tilsvarende.

NTNU, Institutt for energi- og prosesssteknikk

Dato: 3/11 - 2011



Olav Bolland
Instituttleder



Ole Gunnar Dahlhaug
Faglig ansvarlig/veileder

Medveileder:

Preface

This master thesis is written by Simen Røst Breivik at The Waterpower Laboratory at The Norwegian University of Science and Technology, during the spring semester of 2011. The supervisor of the thesis is professor Ole Gunnar Dalhaug. The topic of this thesis is the fluctuating flow in a Francis turbine draft tube at part load. The main goal is to perform a transient CFD analysis of the runner and draft tube at part load, and compare the results with experiences from the model test.

I would like to thank Ole Gunnar Dalhaug, for giving me an interesting challenge and supporting me throughout the entire semester.

I would also like to thank the scientific assistant at the Hydro Power Laboratory, Bjørn Winther Solemslie, for always pointing me in the right direction and providing me with technical documents for this work.

Simen Røst Breivik
20.06.2011

Abstract

This master thesis evaluates the fluctuating flow in a Francis turbine draft tube at part load. The background for studying this subject is partly due to the worlds increased energy demand. With variations in the price of energy and water levels in the reservoirs, Hydro turbines operate at varying loads. Operating at full load and part load causes pressure pulsations in the turbine, with one of the causes being the instability of the draft tube flow. The main goal of this thesis is to perform a CFD analysis of a Francis runner and draft tube operating at part load.

The results from the CFD analysis correspond well with the results from the model test. At the best efficiency point, the draft tube flow is stable and symmetrical in both the model test and CFD analysis. At full load, the flow is also stable and symmetrical, but there is a large low pressure zone below the runner hub. In the model test, the low pressure caused the water to cavitate. At part load the draft tube flow becomes unsteady, and pressure fluctuations were measured. The cork screw shaped vortex rope appears in the draft tube con during the model test. The CFD analysis is single-phase, which means there is no possibility of cavitation, but a pressure Iso-surface reveals a similar cork-screw shape in the draft tube cone.

The pressure frequency measured at part operation correspond well with the theoretical frequency for the same operating point.

Sammendrag

Denne masteroppgaven evaluerer svingningene i sugerørsstrømmingen til en Francis turbin ved dellast. Bakgrunnen for dette studiet er delvis på grunn av verdens økende energibehov. Med varierende energipriser og vannivåer i magasinene opererer vannturbiner på varierende last. Operasjon ved fullast og dellast skaper trykkpulsasjoner i turbinen, hvor en av årsakene er ustabil strømning i sugerøret. Hovedmålet med denne oppgaven er å gjennomføre en CFD-anaøyse av løpehjulet og sugerøret i en Francis turbin ved dellast.

Resultatene fra CFD-analysen stemmer godt overens med modelltesten gjennomført i Vannkraftlaboratoriet. Ved bestpunktet er sugerørsstrømmingen symmetrisk og stabil både i CFD-analysen og i laboratoriet. Ved fullast er sugerørsstrømmingne også symmetrisk og stabil, men det er et stort lavtrykksområde under løpehjulets boss. I laboratoriet kaviterte vannet på grunn av det lave trykket. Ved dellast blir sugerørsstrømmingen ustabil, og trykkpulsasjoner ble målt. En sugerørsvirvel formet som en korketrekker oppstod i sugerørskonusen i laboratoriet. CFD analysen er en-fase, uten mulighet for å kavitere, men en trykkoverflate viser en tilsvarende virvelform i sugerørskonusen.

Frekvensen på trykkpulsasjonene målt ved dellast stemmer godt med den teoretiske frekvensen ved det samme operasjonspunktet.

Contents

Preface	iii
Abstract	v
Sammendrag	vii
List of Figures	xi
List of Tables	xiii
Nomenclature	xvii
1 Introduction	1
2 Francis Turbine	3
2.1 Flow through the runner	3
2.2 Runner Dimensions	6
2.3 Energy conversion	7
2.4 Runner outlet velocity	8
3 Draft Tube	11
3.1 Flow in a draft tube	13
3.2 Boundary layer separation	16
4 Draft Tube Vortex Rope	19
4.1 Flow	19
4.2 Frequency models	24
5 CFD Analysis of Vortex Ropes	29

6	Experimental Methods	35
6.1	Francis turbine test rig	35
6.2	Model test	37
7	Numerical Methods	39
7.1	Geometry	39
7.2	Mesh	42
7.3	Pre-processing	45
7.4	Simulation	51
7.5	Post-processing	52
8	Experimental Results	55
8.1	Hill Chart	55
8.2	Pressure pulsations	55
8.3	Vortex rope	55
9	Numerical Results	59
9.1	Grid Sensitivity Analysis	59
9.2	Steady state simulations	59
9.3	3 second transient simulations	62
9.4	1 second transient simulations	66
9.5	Flow visualization	68
10	Discussion	77
10.1	Flow development	77
10.2	Pressure pulsation frequency	78
10.3	Flow conditions during one period	79
10.4	Comparison with model tests	79
10.5	Comparison with theoretical frequency	79
11	Conclusion	83
12	Further work	85
	Bibliography	87
A	ANSYS CFX	89
A.1	SST Turbulence model	89

List of Figures

2.1	Open Francis turbine.	4
2.2	Relative and absolute flow path in the runner.[1]	5
2.3	Velocity triangles at the inlet and outlet of the runner.[1]	5
2.4	Open Francis turbine.	6
2.5	Energy conversion in a Francis turbine.	8
2.6	Velocity triangle for the outlet at BEP.[1]	9
2.7	Velocity triangle for the outlet at full load.[1]	9
2.8	Velocity triangle for the outlet at part load.[1]	10
3.1	Francis turbine cross section.[1]	12
3.2	Straight diffuser. [1]	13
3.3	Diffuser flow with boundary layer. [1]	15
3.4	Boundary layer separation phenomena. [1]	17
4.1	Flow in the draft tube cone at full load and part load. [1]	19
4.2	Velocity diagram at runner outlet. [2]	22
4.3	A simplified figure of the vortex flow. [3]	25
4.4	Simplified figure of the vortex flow. [3]	26
5.1	Damping effects of the standard κ - ϵ turbulence model. [4]	30
5.2	Varying vortex rope size with time. [4]	31
5.3	Position of pressure measurements in experiment and simulation. [4]	31
5.4	Comparison of experimental and simulated pressure measurements. [4]	32
5.5	Simplified power plant for dynamic simulations. [4]	33
5.6	Results from the dynamic simulation of the power plant. [4]	33
5.7	Schematic procedure for VLES. [4]	34
5.8	Vortex rope comparison between the extended κ - ϵ model and VLES. [4]	34

6.1	Test rig in the laboratory.	35
7.1	The Francis turbine rig in the Waterpower laboratory.	39
7.2	The draft tube geometry from the Tokke model turbine.	40
7.3	The draft tube inlet geometry.	40
7.4	The Tokke model runner geometry.	41
7.5	The runner outlet geometry.	41
7.6	O-grid through the draft tube.	42
7.7	Total draft tube mesh.	42
7.8	The final runner mesh.	43
7.9	The meshing process for the runner.	44
7.10	Runner and draft tube assembly in CFXPre.	45
7.11	Rotating domain in CFXPre.	46
7.12	Smooth wall boundaries of the runner in CFXPre.	47
7.13	Inlet boundary in CFXPre.	47
7.14	Stationary domain in CFXPre.	48
7.15	Outlet boundary in CFXPre.	49
7.16	Domain interface between runner and draft tube in CFXPre.	49
7.17	Cross section of the draft tube in the ZX plane at Y=0.	52
7.18	Cross sections through the draft tube.	53
7.19	Cone cross section.	54
7.20	Polylines and points on the draft tube wall.	54
8.1	Hill chart for the Tokke model turbine.	56
8.2	FFT of the pressure pulsations measured in 2007.	57
8.3	Vortex ropes during the model test.	58
9.1	Grid sensitivity analysis for the runner and draft tube.	60
9.2	Pressure measurements through the draft tube at part load.	62
9.3	Pressure measurements through the draft tube at BEP and full load.	63
9.4	Wall pressure through the draft tube.	64
9.5	Surface pressure through the draft tube.	65
9.6	Pressure in the draft tube cone at part load.	66
9.7	Pressure in the draft tube cone at BEP and full load.	67
9.8	Velocity streamlines leaving the runner.	70
9.9	Pressure contour at the cross section of the draft tube.	71
9.10	Velocity contour at the cross section of the draft tube.	72
9.11	Velocity vectors at the cross section of the draft tube.	73
9.12	Pressure, Velocity, and Vectors in the cone cross section.	74
9.13	Pressure Iso-surface at -77 kPa in the draft tube.	75
10.1	Pressure measurements in the draft tube cone at part load.	77

10.2	Period of pressure pulsation.	78
10.3	Pressure contour in cone cross section at through one period. . . .	80
10.4	Draft tube vortex rope during model test.	81
10.5	Draft tube vortex rope in CFX.	82

List of Tables

7.1	Operating conditions from the Hill chart.	45
7.2	RPM values for the operating points in CFXPre.	46
7.3	Mass flow values for the operating points in CFXPre.	47
7.4	Inlet velocity components for the operating points in CFXPre. . .	48
7.5	Simulations performed in CFX.	51
9.1	Pressure measurements from the steady state simulations.	61
A.1	SST model coefficients	90

Nomenclature

Symbols

t	Time	[s]
Q	Discharge	[m^3/s]
g	Gravitational constant	[m/s^2]
H	Head	[m]
c	Absolute velocity	[m/s]
u	Tangential velocity	[m/s]
w	Relative velocity	[m/s]
D	Diameter	[m]
B	Height	[m]
r	Radius	[m]
M	Momentum	[Nm]
P	Power	[W]
E	Specific hydraulic energy	[J/kg]
A	Area	[m^2]
p	Pressure	[Pa]
C_{pid}	Ideal pressure recovery coefficient	
C_p	Pressure recovery factor	
U	Velocity	[m/s]

Greek letters

ρ	Density	$[kg/m^3]$
ω	Angular velocity	$[rad/s]$
α	Guide vane angle	$[^\circ]$
β	Flow angle	$[^\circ]$
η_h	Hydraulic efficiency	
η_{DT}	Draft tube efficiency	
δ	Boundary layer thickness	$[m]$
ϵ	Turbulent dissipation rate	$[m^2/s^3]$
κ	Turbulent kinetic energy	$[m^2/s^2]$
ω	Turbulence frequency	$[1/s]$

Superscripts

*	Condition at BEP
---	------------------

Subscripts

0	Wicket gate outlet
1	Runner inlet
2	Runner outlet
3	Draft tube outlet
m	Meridian (Runner), Axial (Draft Tube)
u	Tangential

Abbreviations

BEP	Best Efficiency Point
DES	Detached Eddy Simulation

MoC	Method of Characteristics
CFD	Computational Fluid Dynamics
VLES	Very Large Eddy Simulation
rpm	Revolutions per minute
rps	Revolutions per second
FFT	Fast Fourier Transform

Chapter 1

Introduction

The increasing consumption of energy results in hydro turbines operating at varying loads. Francis turbines operating at full and part load experience pressure pulsations that can potentially damage the turbine, at great cost to the owner. One of the causes of pressure pulsations in a Francis turbine is the unstable.

The purpose of this thesis is to evaluate the fluctuating flow in a Francis turbine draft tube. A model test of the Tokke test turbine is performed in the Waterpower Laboratory at NTNU. The draft tube flow is examined at three operating points: the BEP, full load, and part load. A CFD analysis is then performed at the same operating points.

The Tokke test turbine is designed at NTNU. The draft tube is a model scale draft tube from Tokke Kraftverk. 3D models of the runner and draft tube are created in ANSYS ICEM CFD. Structured meshes of the runner and draft tube are created separately. In ANSYS CFX, the runner and draft tube are assembled, and the boundary conditions and initial conditions of each operating point is defined. There are three simulations for each operating point: steady state, 3 second transient analysis starting with no flow in the draft tube, and a 1 second transient analysis starting with the last results from the three second transient analysis. The hybrid turbulence model SST is used, with a high resolution advection scheme, and the upwind transient scheme. Pressure measurements are taken at the surface, wall, and at a point on 9 cross sections through the draft tube to evaluate flow stability. The final analysis of pressure fluctuation is done with pressure measurements taken in the draft tube cone.

The draft tube flow is visually compared to the flow conditions experienced during the model test. The frequency of the measured pressure fluctuations at part load

are compared with the theoretical frequency of the same operating conditions.

This thesis does not focus on the runner. Computational capacity limited a detailed flow analysis of both the runner and the draft tube, so the runner in the CFD analysis is merely used as an instrument to create a realistic velocity profile at the draft tube inlet. As the draft tube vortex rope is a flow phenomenon occurring close to the core of the draft tube cone, the Y^+ of the mesh is not sufficiently low for an accurate solution of the boundary layer flow. Due to the time consumption of a detailed transient CFD analysis, turbulence models, advection schemes, and time schemes are not evaluated.

Chapter 2

Francis Turbine

A Francis turbine is a reaction turbine, utilizing a drop in pressure from inlet to outlet of the runner. A Francis turbine consists of the spiral casing, wicket gate, runner and draft tube. Figure 2.1 shows a complete Francis turbine, with only the cone of the draft tube visible. The stay vanes in the spiral casing distribute the flow evenly around the wicket gate. The wicket gate, consisting of adjustable guide vanes control the discharge, as well as the direction of the flow entering the runner. The flow is constantly accelerated through the spiral casing, due to the decrease in area. The stay vanes and guide vanes rotate the flow, so it enters the runner at an angle rotating about the runner shaft. All the power conversion takes place in the runner. The water flows out of the runner with little or no rotation, and reduced pressure compared to the inlet. The runner converts the kinetic and potential energy in the water into mechanical energy transferred to the runner shaft.

2.1 Flow through the runner

The absolute velocity of the flow is c . The flow is described using a local coordinate system, $(\vec{m}, \vec{n}, \vec{u})$, where \vec{u} is in the direction of the runner rotation, \vec{m} is tangential to the flow streamline, and \vec{n} is normal to the flow streamline. Further, the absolute flow velocity is broken down in equation (2.1).

$$\vec{c} = \vec{u} + \vec{w} \quad (2.1)$$

where \vec{u} is in the tangential direction, and \vec{w} is in the runner blade direction. The absolute velocity can also be expressed by its components in the tangential

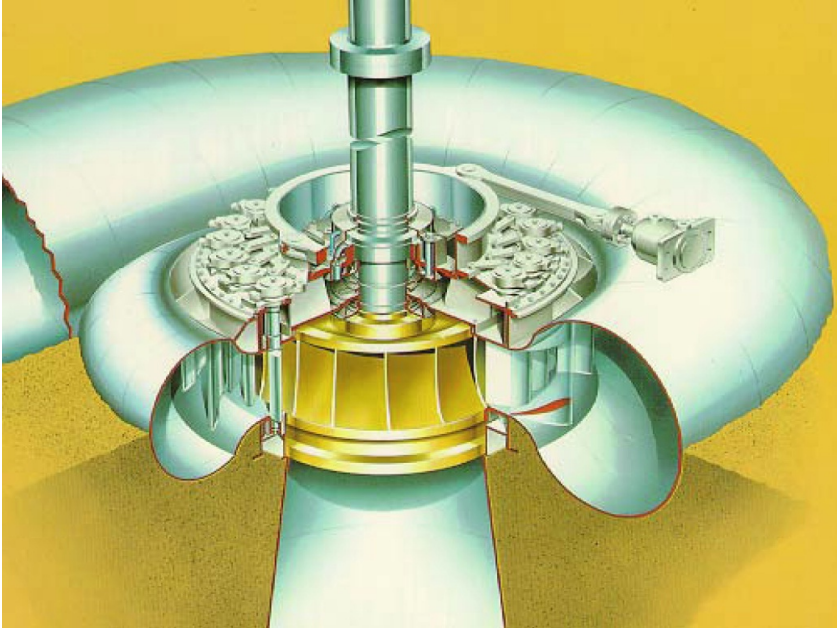


Figure 2.1: Open Francis turbine.

and meridian direction, as in equation (2.2).

$$c_1 = \sqrt{c_{u1}^2 + c_{m1}^2} \quad (2.2)$$

This is shown in figure 2.2. The angle between the absolute velocity \vec{c} and its component in the u-direction, \vec{c}_u , is called α . α is the outlet angle of the flow from the guide vanes. β_1 is the inlet angle of the flow to the runner.

Figure 2.3 shows the velocity triangles of a Francis runner at the inlet and outlet. β_2 is the outlet angle of the flow leaving the runner.

$$\tan \beta_2 = \frac{c_{m2}}{u_2} \quad (2.3)$$

A Francis runner is designed so the runner geometry matches the angles of the flow in a desired operating condition.

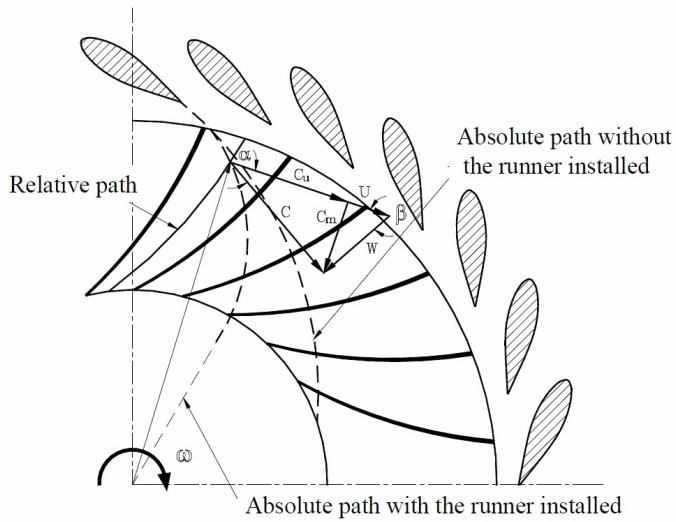


Figure 2.2: Relative and absolute flow path in the runner.[1]

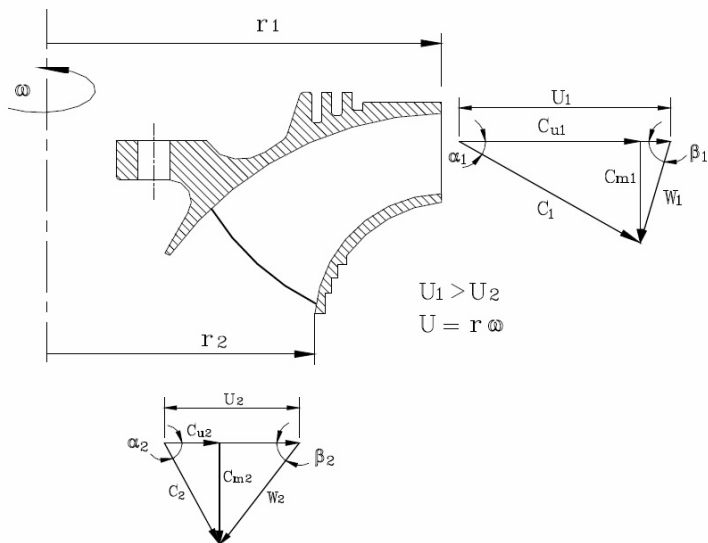


Figure 2.3: Velocity triangles at the inlet and outlet of the runner.[1]

2.2 Runner Dimensions

Figure 2.4 shows the general dimensions of a Francis runner. B_0 is the height of the guide vanes, D_1 is the runner inlet diameter, and D_2 is the runner outlet diameter.

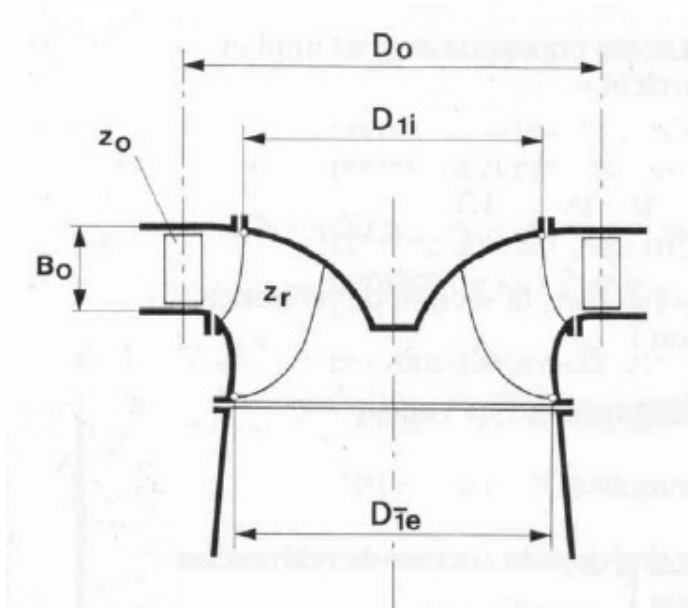


Figure 2.4: Open Francis turbine.

2.2.1 Geometry and flow relations

The discharge and dimensions of the runner can be used to express the flow in the turbine. Equation (2.4), defines the meridian velocity as a function of discharge, inlet diameter, and guide vane height.

$$c_{m1} = \frac{Q}{\pi D_1 B_1} \quad (2.4)$$

The meridian velocity at the outlet is defined in equation (2.5):

$$c_{m2} = \frac{4^*Q}{\pi D_2^2} \quad (2.5)$$

The tangential velocity at the runner outlet is expressed as a function of rotational speed and the outlet diameter in equation (2.6):

$$u_2 = \frac{\pi D_2 n}{60} \quad (2.6)$$

The tangential velocity is a function of radius and rotational speed, expressed in equation (2.7):

$$u = r \cdot \omega \quad (2.7)$$

2.3 Energy conversion

Figure 2.5 shows the energy conversion in a Francis turbine. Half the specific total energy at the inlet of the runner is kinetic energy. The energy is converted to the runner shaft, and the draft tube converts the remaining kinetic energy into static pressure.

The momentum exerted on the runner is expressed as:

$$\vec{M}_z = \dot{m} (c_{1u}r_1 - c_{2u}r_2) = \rho Q (c_{1u}r_1 - c_{2u}r_2) \quad (2.8)$$

The power transfered to the runner shaft is:

$$P = M_z \omega = \rho Q (c_{1u}r_1 - c_{2u}r_2) \omega = \rho Q E_t = \rho Q g H_n \quad (2.9)$$

where E_t is defined as the specific energy transfered from the water to the runner:

$$E_t = \omega (c_{1u}r_1 - c_{2u}r_2) = c_{1u}u_1 - c_{2u}u_2 \quad (2.10)$$

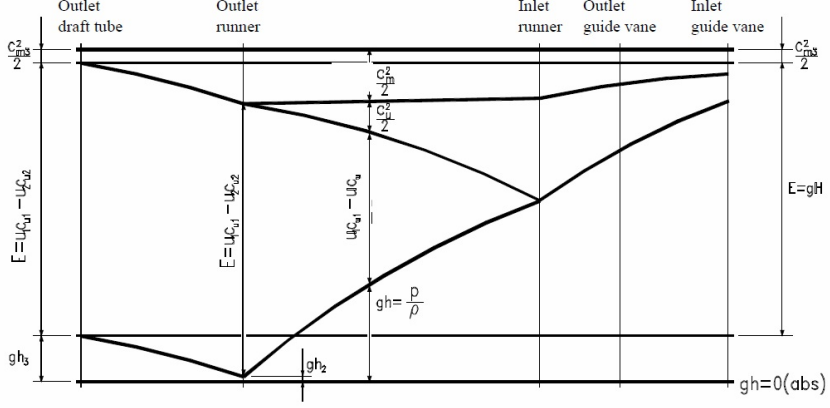


Figure 2.5: Energy conversion in a Francis turbine.

The total available energy in the runner is:

$$gH_n = \left(gh_1 + \frac{c_1^2}{2} \right) - \left(gh_3 + \frac{c_3^2}{2} \right) \quad (2.11)$$

The hydraulic efficiency of the runner is the ratio of energy converted compared to the available energy. By using equations (2.10) and (2.11), the hydraulic efficiency can be expressed as:

$$\eta_h = \frac{1}{gH_n} (c_{1u}u_1 - c_{2u}u_2) \quad (2.12)$$

Equation (2.12) is called the Euler turbine equation. It neglects viscous and turbulent losses in both the runner and the draft tube, and the calculated efficiencies are very high.

2.4 Runner outlet velocity

The velocity exiting the runner depends on the operating conditions of the turbine.

2.4.1 Best Efficiency Point

At the best efficiency point, the BEP, the flow leaving the runner has little or no rotation. In theory, c_{2u} is zero at the BEP. Figure 2.6 shows the outlet velocity triangle at the BEP.

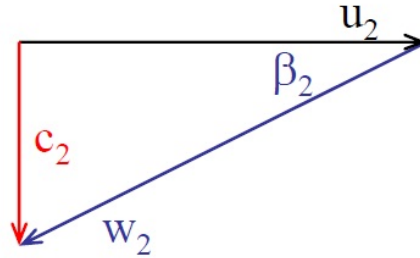


Figure 2.6: Velocity triangle for the outlet at BEP.[1]

2.4.2 Full load

At full load, the runner is unable to utilize all the rotation in the flow. The flow leaving the runner has a reduced rotation in the same direction as the flow entering the runner. Figure 2.7 shows the outlet velocity triangle for a runner at full load. The flow entering the draft tube is rotating in the opposite direction of the runner.

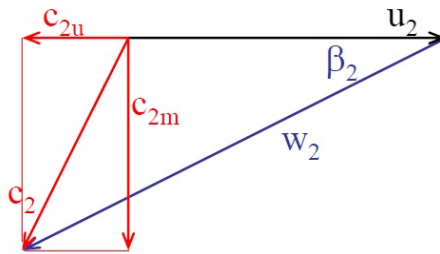


Figure 2.7: Velocity triangle for the outlet at full load.[1]

2.4.3 Part load

At part load the rotation in the flow is reversed. The flow entering the draft tube rotates in the same direction as the runner. Figure 2.8 shows the outlet velocity triangle for a runner at part load.

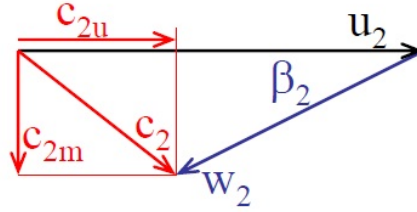


Figure 2.8: Velocity triangle for the outlet at part load.[1]

Chapter 3

Draft Tube

A hydro power plant converts the potential energy between two water surfaces into to mechanical or electrical energy. In a Francis turbine, the flow leaving the runner has kinetic energy that can be utilized. To recover this kinetic energy, the runner outlet is connected to a draft tube. The main task of the draft tube is to convert the kinetic energy at the outlet of the runner into static pressure. The industry standard is to have a vertical runner axis, as in figure 3.1. Due to high construction costs, the draft tubes are normally bent at an elbow. The cross section of the draft tube inlet is circular. As the water flows through the draft tube, the cross section become elliptic and later rectangular with rounded corners.

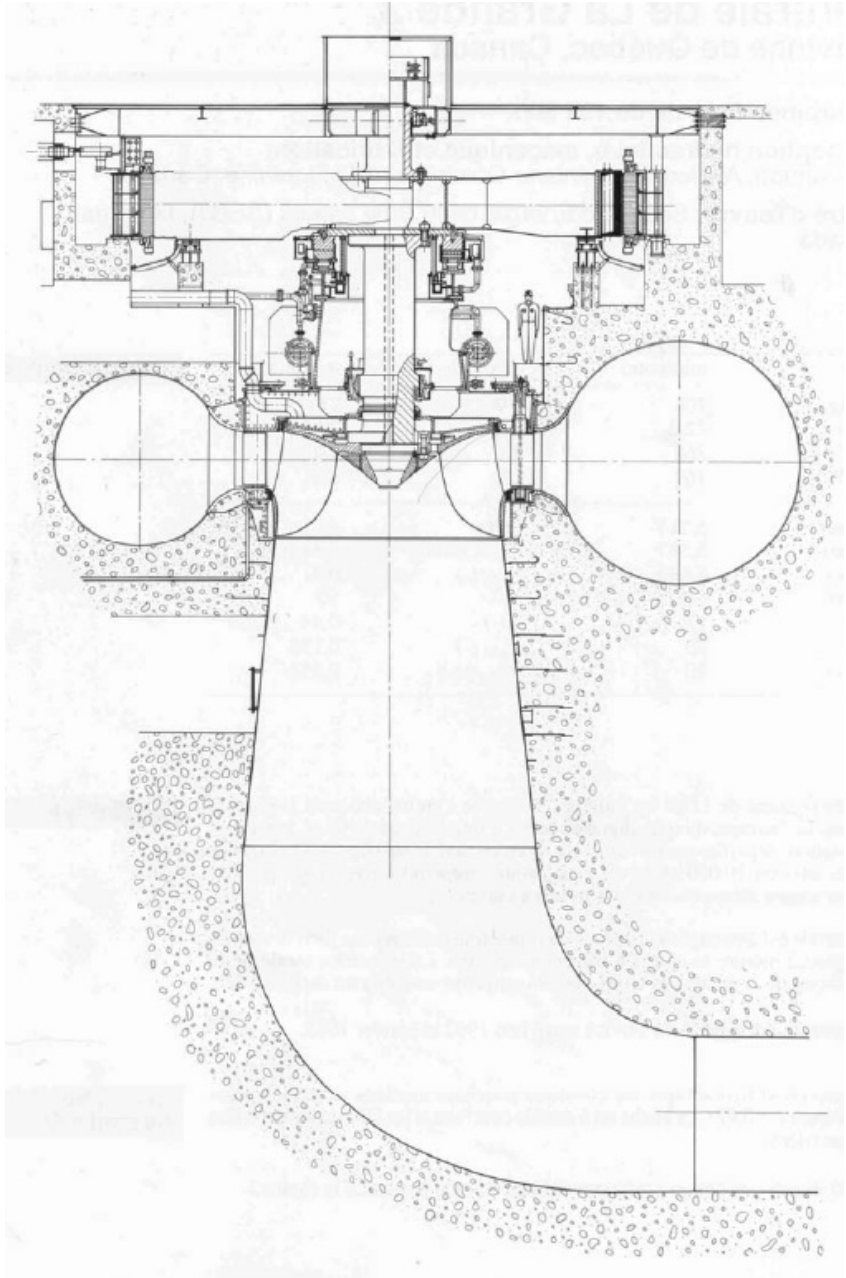


Figure 3.1: Francis turbine cross section.[1]

3.1 Flow in a draft tube

The flow in a draft tube is complex. The draft tube geometry creates further difficulties in describing the flow. By straightening the draft tube, and assuming circular cross sections through the entire draft tube, it becomes a diffuser. The pressure recovery concept of the draft tube is better explained assuming it is shaped as a straight diffuser.

3.1.1 Uniform flow in a diffuser

Assume the runner is operating at the BEP:

$$c_{2u} = 0 \quad (3.1)$$

Assuming no radial velocity, the flow is uniform at the inlet of the diffuser. The uniform flow can be seen in figure 3.2.

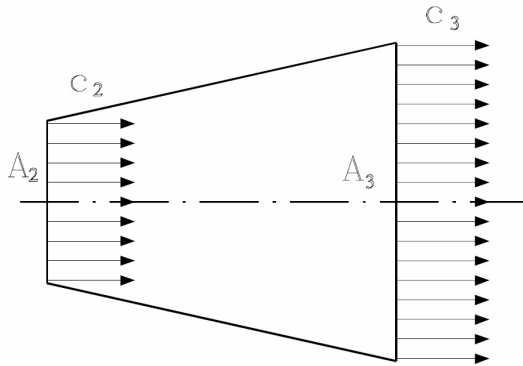


Figure 3.2: Straight diffuser. [1]

[5] By rearranging the continuity equation the outlet velocity can be expressed as:

$$c_3 = \frac{A_2}{A_3} c_2 \quad (3.2)$$

Neglecting losses, and assuming the diffuser is horizontal, the incompressible Bernoulli equation states:

$$p_2 + \frac{1}{2}\rho c_2^2 = p_3 + \frac{1}{2}\rho c_3^2 = \text{constant} \quad (3.3)$$

Inserting the velocity expression from equation (3.2) and dividing by ρ , equation (3.3) becomes:

$$\frac{p_3 - p_2}{\rho} = \frac{1}{2}(c_2^2 + c_3^2) = \frac{c_2^2}{2} \left(1 - \left(\frac{A_2}{A_3} \right)^2 \right) \quad (3.4)$$

The ideal pressure recovery coefficient of a draft tube, C_{pid} , is defined as:

$$C_{pid} = 1 - \left(\frac{A_2}{A_3} \right)^2 \quad (3.5)$$

By introducing losses to equation 3.4, it states:

$$\frac{p_3 - p_2}{\rho} = \frac{1}{2}(c_2^2 + c_3^2) - \xi \frac{c_2^2}{2} = \frac{c_2^2}{2} \left(1 - \left(\frac{A_2}{A_3} \right)^2 \right) - \xi \frac{c_2^2}{2} = \eta_{DT} \frac{c_2^2}{2} C_{pid} \quad (3.6)$$

where η_{DT} is the draft tube efficiency, defined as:

$$\eta_{DT} = 1 - \frac{\xi \frac{c_2^2}{2}}{\frac{c_2^2}{2} C_{pid}} \quad (3.7)$$

The actual pressure recovery factor, C_p , is defined as:

$$C_p = \frac{p_3 - p_2}{\frac{c_2^2}{2} \rho} \quad (3.8)$$

η_{DT} can be expressed as:

$$\eta_{DT} = \frac{C_p}{C_{pid}} \quad (3.9)$$

which means the draft tube efficiency is the relation between the actual pressure recovery factor and the ideal pressure recovery factor. [1].

The result for an actual draft tube is more complex, because of geometrical differences and different velocity profiles at both inlet and outlet. If turbulence and boundary layers are introduced, the flow in the diffuser will have a velocity profile as displayed in figure 3.3.

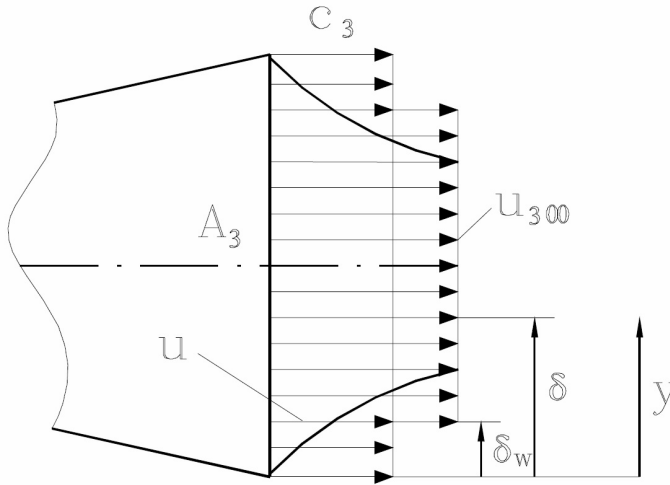


Figure 3.3: Diffuser flow with boundary layer. [1]

The velocity at the wall is 0, and the velocity at the center of the diffuser is U_∞ . Note that U_∞ is greater than the average velocity over the area, c_3 . The area of increasing velocity is called the boundary layer. The boundary layer thickness, δ , is defined as the distance from the wall to where the velocity equals $0.99 U_\infty$. This definition is impractical, because the transition to U_∞ is unstable due to turbulent fluctuations. For mathematical treatment of the boundary layer, a displacement thickness, δ^* , is defined.

$$\delta^* = \int_0^\delta \left(1 - \frac{u}{U_\infty}\right) dy \quad (3.10)$$

where y is the distance from the wall towards the center.

If the area covered by δ^* is omitted, the velocity U_∞ can be treated as the mean velocity over the remaining area, A^* . The definition of A^* is:

$$A^* = A - A\delta^* \quad (3.11)$$

The pressure recovery coefficient from equation 3.8 can now be written as:

$$C_p = 1 - \left(\frac{U_{3\infty}}{U_{2\infty}}\right)^2 = 1 - \left(\frac{A_2}{A_3^*}\right)^2 \quad (3.12)$$

The boundary layer gives the flow a higher velocity at the outlet. This results in a higher energy in the flow, which is not accounted for in the mean velocity calculations.

3.2 Boundary layer separation

The boundary layer theory in the previous section assumes no separation in the diffuser. If the flow does not follow the walls, boundary layer separation occurs. Consider a diffuser with length L , and diffuser angle α . By gradually increasing the diffuser angle, different separation phenomena will occur. The different phenomena are depicted in figure 3.4

1. The flow follows the walls, and no separation occurs. This is the case described in the previous section.
2. The flow experiences an unstable separation, and a temporary eddy is generated. The flow is reattached behind the eddy, and continues to follow the wall.
3. The flow experiences a stable separation. The separation occurs at one wall, and the flow follows the other wall.
4. The flow experiences complete separation. Separation occurs at both walls, and the flow is a free jet between both eddies.

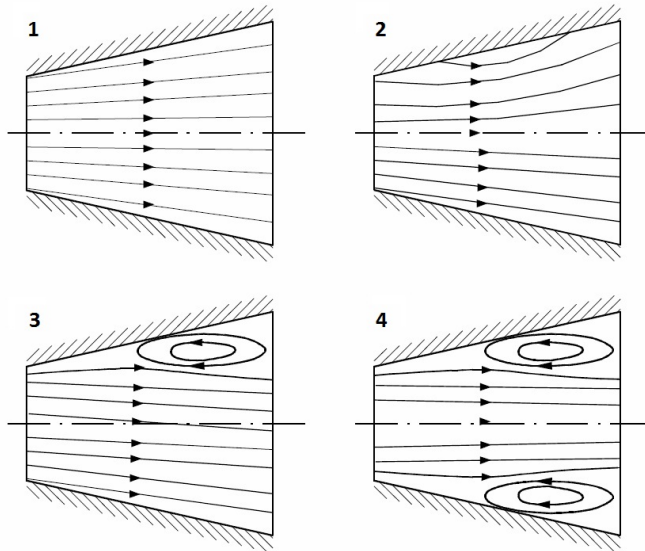


Figure 3.4: Boundary layer separation phenomena. [1]

Chapter 4

Draft Tube Vortex Rope

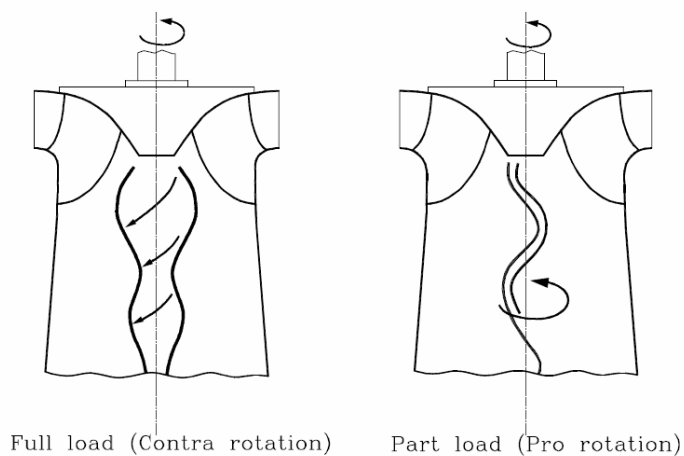


Figure 4.1: Flow in the draft tube cone at full load and part load. [1]

4.1 Flow

At the BEP, the flow leaving the runner has, in theory, no rotation. In practice, there is a small but insignificant amount of swirl in the flow. At part load, the

flow leaving the runner rotates in the same direction as the runner. When the turbine is operating at full load, the flow leaving the runner is rotating in the opposite direction of the runner. This is visible in figure 4.1. If the swirl entering the draft tube is above a certain level, the flow becomes unstable and draft tube surge occurs. Draft tube surge causes pressure fluctuations that can result in vibration, penstock resonance, and power swings.

Pure axial flow through a straight tube is stable as long as the flow is fully turbulent. By introducing rotation to the flow, the flow pattern is changed. The axial velocity decreases in the center, and increases along the walls. The peripheral velocity increases near the walls. A stagnation point is developed, and the flow along the centerline, both upstream and downstream, is directed towards this point. The development of this stagnation point is known as vortex breakdown. Experiments performed by J. J. Cassidy investigated the nature of the vortex breakdown in order to better understand draft tube surging[6]. As the rotation of the flow increases, the stagnation point moves upstream to the outlet of the runner. The flow in the draft tube cone develops into a rotating helical vortex. It is this vortex that causes the pressure fluctuations in the draft tube.

A helical vortex causes asynchronous pressure fluctuations in the draft tube. As high pressure develops on one side of the draft tube, low pressure is simultaneously developed on the opposite side. In a hydro turbine, the pressure can become low enough to cavitate the helical vortex. This creates a visible vortex in the draft tube cone. The vortex rope cavity pulsates, creating synchronous pressure fluctuations in the draft tube. These fluctuations occur at twice the asynchronous frequency [7].

Experiments performed by Yutaka Hosoi show that the precession rate of the draft tube vortex under constant operating conditions remains unchanged. The experiments also show that the draft tube vortex is both rotating and revolving [2]. It is observed that the vibration forces are greater at high load than at partial load.

The sizes of the vortex cores differ depending on the head, flow rate, and runner speed. When the vortex core attains a diameter above a certain size, the top of the spiral vortex becomes an ogival shape core with no whirling. When the vortex core has a small diameter, the length of the spiral is short, and the vortex will appear and disappear irregularly.

4.1.1 Parameters for Describing Draft Tube Surging

The torque entering the runner minus the torque created by the runner equals the moment of momentum of swirl leaving the runner. The torque entering the runner is determined by the geometry of the flow passing through the wicket gates. Equation (4.1) approximates the flux of angular momentum leaving the wicket gates.

$$\Omega_1 = \frac{\rho Q^2 R \sin(\alpha)}{BNS} \quad (4.1)$$

where:

B = height of the wicket gates

N = number of wicket gates

Q = discharge

R = radius to the centerline of the gate opening

S = minimum width of flow passing through the wicket gate

α = angle between the flow vector and the radius

ρ = water density

The speed characteristics of the runner, the discharge, and the head combine to determine the torque produced by the turbine. From this, the swirl leaving the runner can be calculated in (4.2).

$$\frac{\Omega D}{\rho Q^2} = \frac{DR \sin(\alpha)}{BNS} - \frac{P_{11}D}{2\sqrt{2g\rho\Phi Q_{11}^2 D_2^2}} \quad (4.2)$$

The term on the left side of (4.2) is the swirl parameter. Using (4.2) combined with a model test to determine the surge characteristics of a turbine is known as the swirl parameter method. Experiments performed by Falvey and Cassidy [8] showed that surging begins at a swirl parameter of about 0,3.

4.1.2 Rotating flow at turbine outlet

Consider the velocity of the rotational flow forming a vortex core in the draft tube in terms of the velocity streamlines passing through the runner. Based on the velocity diagram in figure 4.2, the velocity may be expressed as:

$$C_u = V_a - W_a \cos \gamma \quad (4.3)$$

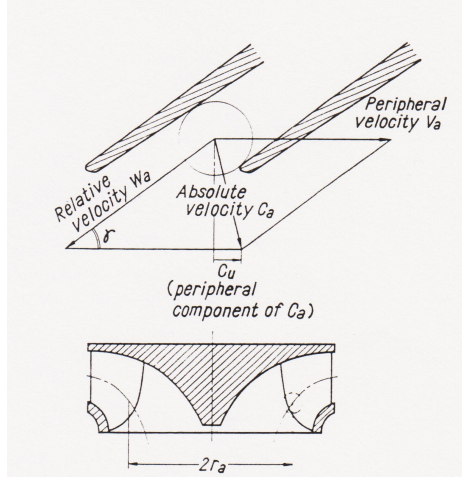


Figure 4.2: Velocity diagram at runner outlet. [2]

where C_u is the peripheral velocity component, V_a is the peripheral velocity of the runner, W_a is the relative velocity of the water flow, and γ is the blade outlet angle. By expressing these quantities in terms of values per unit head, (4.3) becomes:

$$C_{u1} = V_{a1} - W_{a1} \cos \gamma \quad (4.4)$$

where:

$$C_{u1} = \frac{C_u}{\sqrt{H}}$$

$$V_{a1} = \frac{V_a}{\sqrt{H}}$$

$$W_{a1} = \frac{W_a}{\sqrt{H}}$$

H = effective head.

By introducing the expressions:

$$N_1 = \frac{N}{\sqrt{H}}$$

$$Q_1 = \frac{Q}{\sqrt{H}}$$

the following functions are obtained:

$$V_{a1} = \frac{2\pi r_a}{60} N_1$$

$$W_{a1} = \frac{1}{bZ} Q_1$$

where:

r_a = blade outlet radius
 b = sectional area at outlet between blades
 Z = number of blades

From this, (4.4) can be written as:

$$C_{u1} = \frac{2\pi r_a}{60} N_1 - \frac{1}{bZ} \cos \gamma Q_1 \quad (4.5)$$

From this, C_{u1} can be considered a function of N_1 and Q_1 , since $\frac{2\pi r_a}{60}$ and $\frac{1}{bZ} \cos \gamma$ in (4.5) are constant for the turbine runner. This is, however, the theoretical average peripheral velocity component of the runner. Experiments show that as the rotational speed of the flow leaving the runner increases, the effects of the centrifugal forces increase. The water is forced towards the draft tube walls, and a ineffective area is generated in the center of the draft tube. Experiments performed by Yutaka Hosoi show the difference between theoretical and actual rotational flow exiting the runner [2].

4.2 Frequency models

Further experiments performed by Yutaka Hosoi, focusing on pressure surges in the draft tube, show a breakdown of the pressure fluctuations measured in a Francis turbine model rig at different operating points. The results showed two pressure fluctuations with a natural frequency corresponding with the revolution speed of the pump in the test rig. These high frequency, low amplitude fluctuations were excluded from the analysis. The third fluctuation had a low-cycle frequency and a varying amplitude depending on the operating conditions of the turbine. These pressure fluctuations reached amplitudes that influenced the penstock pressure at a defined value of N_1 depending on the gate opening. These results correspond well with the theory of pressure fluctuations as a function of the peripheral velocity from the outlet of the runner [2].

To express the frequency in terms of quantity per unit head:

$$n_1 = \frac{n}{\sqrt{H}} \quad (4.6)$$

Frequency in Heavy Pressure Surge

After analyzing the results, Hosoi expressed a relation between the pressure surges in the draft tube and the runner speed:

$$n_1 = \frac{N_1}{3} \frac{1}{60} [\text{cycles per second}] \quad (4.7)$$

where:

$$n_1 = \text{c/s per unit head.}$$

$$N_1 = \text{rpm per unit head.}$$

This conclusion corresponds well with the empirical results collected by Rheingans [9] in 1940, who published the following formula after examining several power plants experiencing heavy pressure surges:

$$f = \frac{n}{c} \quad (4.8)$$

where:

$$\begin{aligned} f &= \text{surge frequency, cycles per second} \\ n &= \text{runner speed, rotations per second} \\ 3, 2 \leq c \leq 4, 0 \end{aligned}$$

4.2.1 Mathematical model

The flow conditions of the draft tube vortex were investigated by Michele Fanelli, who made a simplified model shown in figure 4.3. From the simplified model, the following equations can be derived from the geometry in figure 4.4.

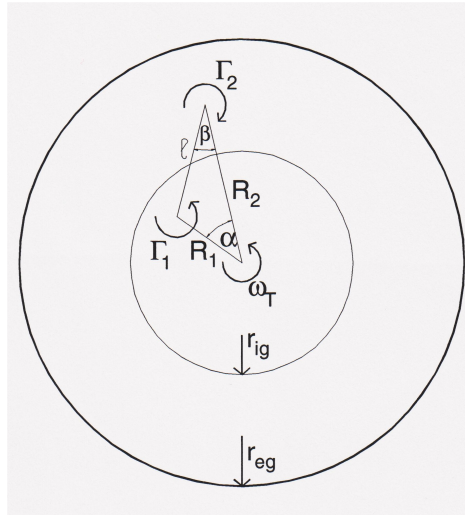


Figure 4.3: A simplified figure of the vortex flow. [3]

$$\frac{R_1}{\sin \beta} = \frac{\ell}{\sin \alpha} \quad (4.9)$$

$$\frac{R_2}{\sin (\alpha + \beta)} = \frac{\ell}{\sin \alpha} \quad (4.10)$$

$$\ell = \sqrt{R_1^2 + R_2^2 - 2R_1R_2 \cos \alpha} \quad (4.11)$$

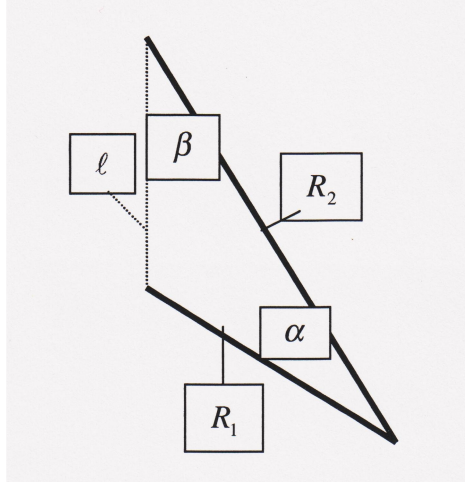


Figure 4.4: Simplified figure of the vortex flow. [3]

Assuming the vortex filaments have no radial velocity, their kinematical conditions are described by the following equations:

$$\frac{\Gamma_2}{2\pi\ell} \sin(\alpha + \beta) = \frac{Q}{2\pi R_1 h} \quad (4.12)$$

$$\frac{\Gamma_1}{2\pi\ell} \sin \beta = \frac{Q}{2\pi R_2 h} \quad (4.13)$$

where:

$$\begin{aligned} Q &= nQ_0 \\ n &< 1 \\ Q_0 &= \text{discharge resulting in zero swirl} \end{aligned}$$

If the two vortices have the same angular velocity, the formulas is:

$$\omega_T = \frac{1}{R_1} \frac{\Gamma_2}{2\pi\ell} \cos(\alpha + \beta) = \frac{1}{R_2} \frac{\Gamma_1}{2\pi\ell} \cos\beta \quad (4.14)$$

m is a non-dimensional coefficient:

$$m = \frac{Q_0}{2\pi h r_{ig}^2 \omega_0} \quad (4.15)$$

where:

$$\begin{aligned} r_{ig} &= \text{runner outlet radius} \\ \omega_0 &= \text{runner angular velocity} \\ m &< 1 \end{aligned}$$

Quantification of outlet circulation Γ_1 :

$$\Gamma_1 = 2\pi r_{ig}^2 (1 - n) \omega_0 \quad (4.16)$$

From these equations, the following relationships can be derived:

$$\rho = \frac{R_2}{R_1} = \sqrt{1 + \frac{1 - n}{nm}} \quad (4.17)$$

$$\frac{\omega_T}{\omega_0} = (1 - n + nm) \left(\frac{r_{ig}}{R_2} \right)^2 \quad (4.18)$$

$$\alpha = \frac{\pi}{2} - 2\beta \quad (4.19)$$

$$\beta = \arcsin \sqrt{\frac{nm}{1 + (2m - 1)n}} \quad (4.20)$$

$$\frac{\Gamma_2}{\Gamma_1} = 1 \tag{4.21}$$

Fanelli found through mathematical modeling that the angular velocity of the vortex rope varies between 0,3 and 0,35 times the angular velocity of the runner. This corresponds well with the model in equation (4.8).

Chapter 5

CFD Analysis of Vortex Ropes

Simulations performed by Ruprecht et al. [4] shows the influence and importance of the turbulence model. A Francis runner was simulated in steady state at part load, and the resulting outlet velocity profile was set as the inlet of the draft tube. Constant pressure at the outlet of the draft tube was assumed. The simulations were done in FENFLOSS, based on the RANS-equations. The standard $\kappa - \epsilon$ turbulence model had a strong damping, and no vortex rope appeared. When using the extended Kim & Chen $\kappa - \epsilon$ turbulence model, the vortex rope appeared. Figure 5.1 shows the effects of turbulence damping in the simulations. The extension of the turbulence model consists of an additional term in the ϵ -equation, shown in (5.1).

$$\frac{\partial \epsilon}{\partial t} + U_j \frac{\partial \epsilon}{\partial x_j} = \frac{\partial}{\partial x_j} \left(\left(\nu + \frac{\nu_t}{\sigma_\epsilon} \right) \frac{\partial \epsilon}{\partial x_j} \right) + C_{1\epsilon} \frac{\epsilon}{\kappa} P_\kappa - C_{2\epsilon} \frac{\epsilon^2}{\kappa} + \underbrace{C_{3\epsilon} \left(\frac{P_\kappa}{\kappa} \right) P_\kappa}_{\text{extension term}} \quad (5.1)$$

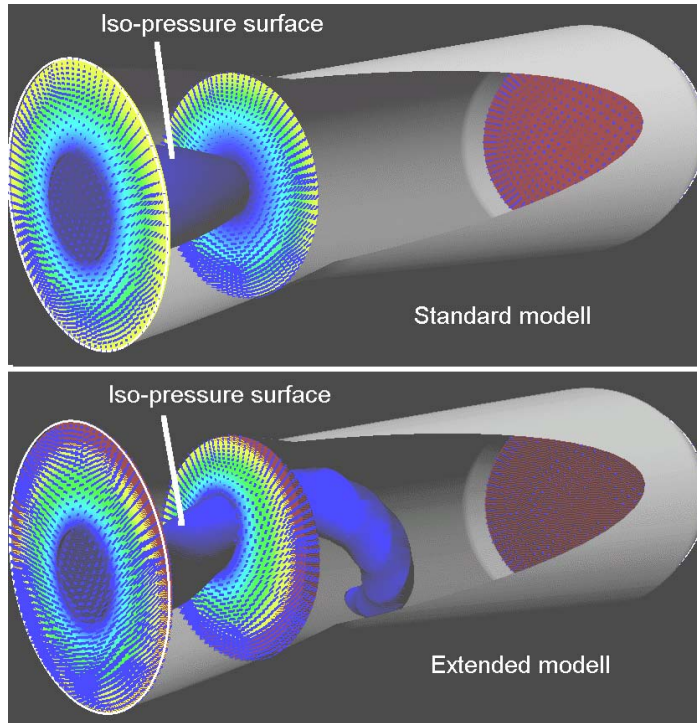


Figure 5.1: Damping effects of the standard κ - ϵ turbulence model. [4]

The results from the simulation using the Kim & Chen $\kappa - \epsilon$ turbulence model show unsteady flow behavior in the draft tube. The resulting vortex rope has the shape of a rotating cork-screw. The change in size of the vortex rope over time indicates pressure surges in the draft tube. This means the draft tube is subjected to synchronous pressure fluctuations. This effect is shown in figure 5.2.

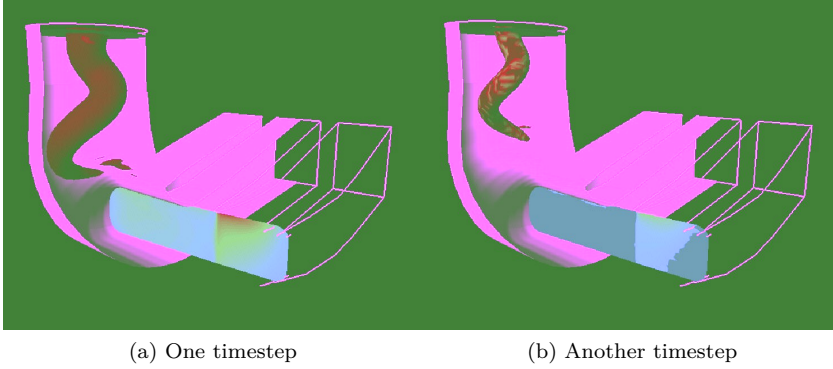


Figure 5.2: Varying vortex rope size with time. [4]

To verify the simulations, the pressure is measured at the same location in the experiment and simulations, shown in figure 5.3.

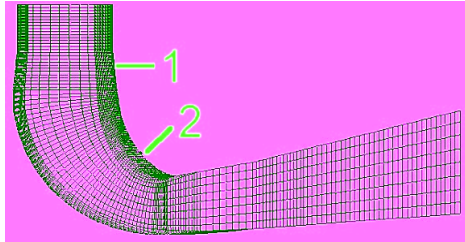


Figure 5.3: Position of pressure measurements in experiment and simulation. [4]

As expected, the frequency of the pressure fluctuations are similar. The amplitude of the pressure fluctuations decreases in as the distance from the inlet increases. This is most likely due to damping of the swirl in the simulations. A Fast Fourier Transformation is performed on the measured and simulated values. The dominating frequency is 7 Hz, which is the frequency of the vortex rope. It is 33% of the runner speed. The numerical comparison is shown in figure 5.4.

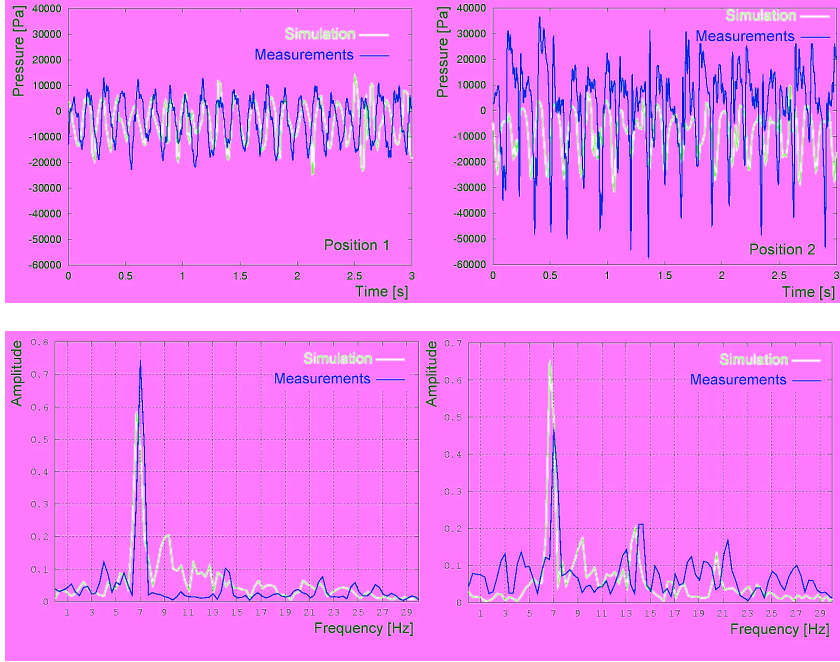


Figure 5.4: Comparison of experimental and simulated pressure measurements. [4]

The pressure fluctuations in the draft tube causes oscillations in the water passage of the power plant. This results in a time dependent variation in the discharge. This is not taken into account in a steady state runner simulation, and therefore the draft tube simulations are not accurate. To include the dynamic behavior of the power plant in the simulations, a simple power plant is considered. The power plant, shown in figure 5.5, consists of upper basin, penstock, turbine, draft tube and lower basin.

By using the 1-D Method of Characteristics, the dynamic behavior of the penstock is calculated. The turbine is represented by its linearized steady state hill chart, and the draft tube is simulated with CFD. The pressure at the draft tube inlet is averaged in each time step of the transient CFD analysis, and used as a boundary condition in the MoC. The MoC results in a new value for the discharge, which is reintroduced to the CFD simulation as a change in the axial velocity. This coupled simulation leads to a synchronous pressure oscillation of approximately 3% and a resulting discharge variation of approximately 1%. The time dependent fluctuations in pressure and discharge are shown in figure 5.6.

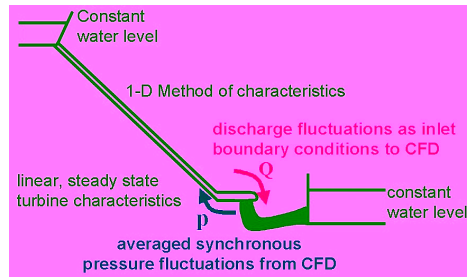


Figure 5.5: Simplified power plant for dynamic simulations. [4]

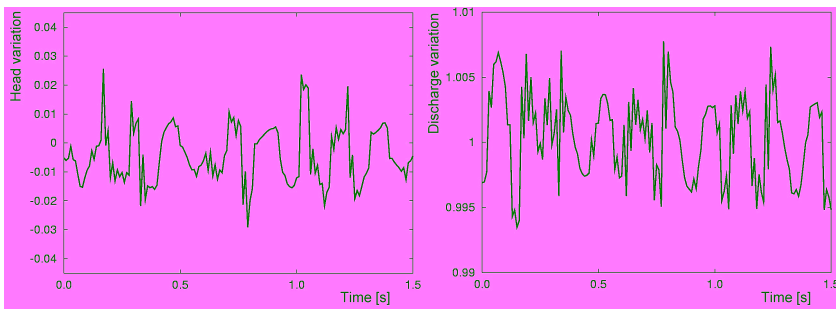


Figure 5.6: Results from the dynamic simulation of the power plant. [4]

Ruprecht et al. [4] concluded that the damping of the turbulence model used in the simulation greatly affect the prediction of vortex ropes. An improved turbulence model is necessary to obtain accurate simulation results. When applying Large Eddy Simulation (LES) to a simulation, large parts of the turbulent spectrum have to be resolved by the computation. This is impossible for high Reynolds numbers. A simpler approach to LES, Very Large Eddy Simulation (VLES) only solves the dominant frequencies, and most of the turbulent spectrum is modeled. This is schematically shown in figure 5.7.

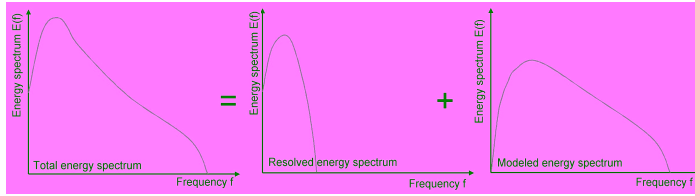


Figure 5.7: Schematic procedure for VLES. [4]

By using the same method of comparing turbulence models as in figure 5.1, the extended $\kappa - \epsilon$ turbulence model is compared to the VLES approach. The result is visible in figure 5.8.

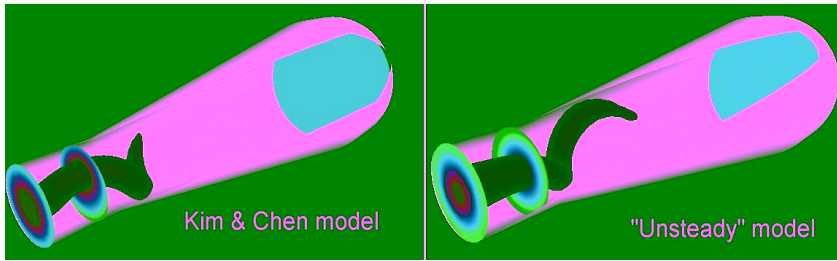


Figure 5.8: Vortex rope comparison between the extended $\kappa - \epsilon$ model and VLES. [4]

Chapter 6

Experimental Methods

6.1 Francis turbine test rig

When performing a model test on a Francis turbine, the water flows through a closed loop. Figure 6.1 shows the main parts of the test rig. The water is pumped to the pressure tank on the left. It then passes through the turbine and into the reservoir tank downstream the turbine. From the reservoir, the water flows back to the pump to complete the cycle. The Francis rig is according to IEC 60193.

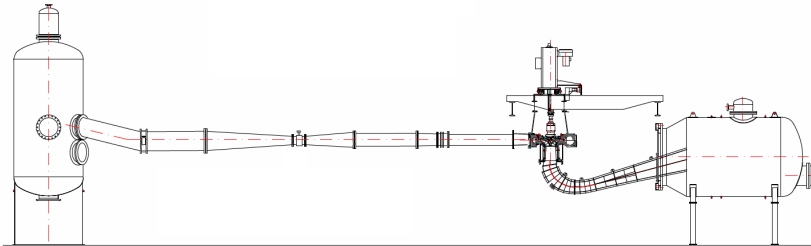


Figure 6.1: Test rig in the laboratory.

6.1.1 Measuring instruments

Generator

The generator is connected to a DC converter, which is connected to the power grid. This enables the operator to choose the operating point of the turbine by

altering the rpm with a change in power to the generator. The generator is not used to measure the energy output of the turbine, as this is done with torque measurements.

RPM

The rpm of the turbine is measured by an optical sensor on the shaft between the runner and the generator.

Torque

The rig has two torque measurements, generator torque and friction torque. Both torques are measured by multiplying force with arm length. The force is measured by a load cell transmitting an electrical current corresponding to the force. The effect of the measured torque is given by the torque multiplied with the speed of rotation of the turbine. Both the torque measuring cells must be calibrated before a model test.

Flow

The flow is measured with an electromagnetic flow meter at a known cross section upstream the turbine. A magnetic field is created by two magnetic coils, and the fluid acts as a conductor. The signal given out by the flow meter is proportional to the velocity. The flow meter must be calibrated before a model test, using the calibration tank in the laboratory.

Pressure

Pressure is measured at the inlet and the outlet of the turbine. The absolute pressure is measured at the inlet, and the pressure difference from inlet to outlet is measured at the outlet. Both the pressure transducers must be calibrated before a model test.

Oxygen

The oxygen content of the water is measured between the reservoir tank and the pumps. The sensor measures the amount of dissolved oxygen.

Temperature

The temperature of the water is measured upstream the turbine.

6.2 Model test

The model test is performed with a $H_n = 10m$. When performing a model test in the laboratory, the test starts at the turbines BEP. The guide vane opening is then set to a predetermined angle, and the rpm of the turbine is altered to log information at different operating points. As the turbine rpm is changed, the pump rpm must be changed in order to maintain a 10 meter net head. The logging procedure for each guide vane angle is to start at the rpm of the BEP, and reduce the turbine rpm in small increments. The same operating points are measured on the way back to the BEP rpm. The turbine rpm is then increased in small increments, and the operating points are logged coming from and going to the BEP rpm.

6.2.1 Guide vane openings

The following guide vane openings are evaluated:

- $\alpha = 6^\circ$
- $\alpha = 7^\circ$
- $\alpha = 8^\circ$
- $\alpha = 9^\circ$
- $\alpha = 10^\circ$
- $\alpha = 11^\circ$
- $\alpha = 12^\circ$
- $\alpha = 13^\circ$
- $\alpha = 14^\circ$

Chapter 7

Numerical Methods

7.1 Geometry

The geometry used in the simulations is in the same scale as the model turbine in the laboratory, which can be seen in figure 7.1. The geometry of the draft tube and runner are generated separately.

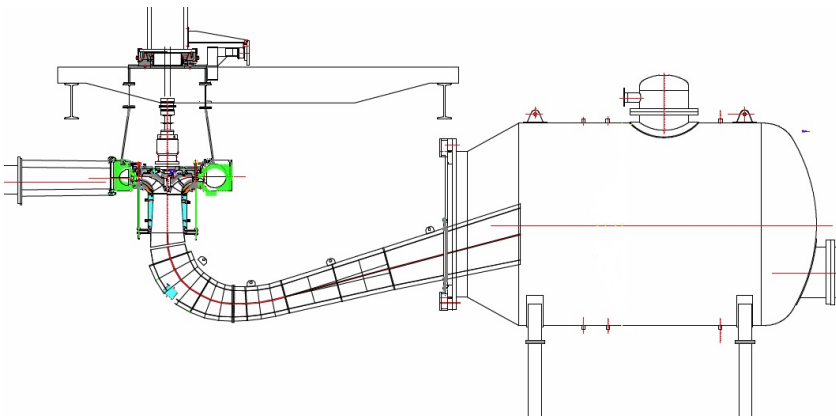


Figure 7.1: The Francis turbine rig in the Waterpower laboratory.

7.1.1 Draft Tube

By using technical drawings of the draft tube, it is regenerated in ANSYS ICEM CFD, and adapted for optimal meshing. The geometry created in ICEM contains only the inner surface of the draft tube. Figure 7.2 shows the 2D AutoCad drawing of the draft tube, and the 3D model created in ICEM based on the technical information of cross section through the geometry.

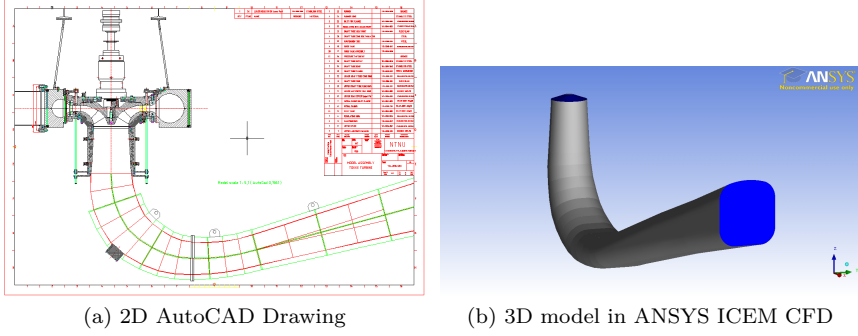


Figure 7.2: The draft tube geometry from the Tokke model turbine.

The inlet of the draft tube, shown in figure 7.3 is not a plane surface. This is done to improve the computation conditions for the model assembly. The center of the inlet is covered with a circular surface, which will be used as the rotating tip of the runner hub. The runner is a rotating domain in the computations, while the draft tube is stationary. By connecting the runner outlet and draft tube inlet close to the runner blades, the effects of the rotating runner domain on the stationary area below the blades is reduced.

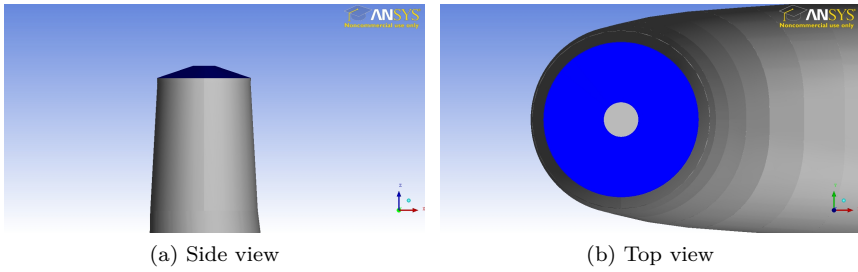


Figure 7.3: The draft tube inlet geometry.

7.1.2 Runner

The runner is designed at the Waterpower Laboratory at NTNU. As the geometry files are not compatible with ANSYS ICEM CFD, the geometry is exported from ProE and regenerated for optimal meshing. Figure 7.4 shows the runner geometry from ProE, and the new geometry created in ICEM. The original geometry contains a detailed geometry of the solid part of the runner, while the new geometry is a detailed geometry of the waterways of the runner.

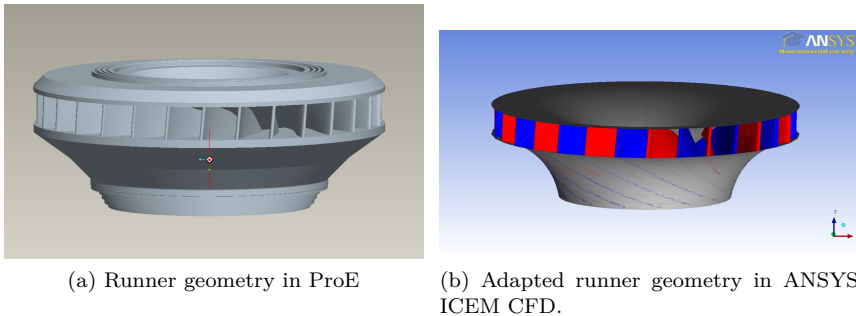


Figure 7.4: The Tokke model runner geometry.

Figure 7.5 shows how the geometry of the runner outlet is created from the tip of the runner hub to the bottom of the shroud. As mentioned earlier, this is to improve the computation conditions of the model assembly. Note the reduced gap between the runner blades and the runner outlet.

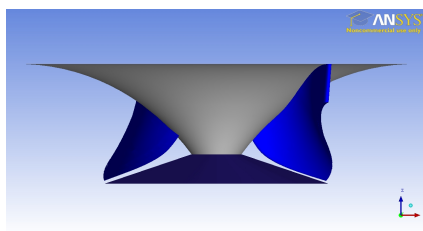


Figure 7.5: The runner outlet geometry.

7.2 Mesh

The geometry is meshed with a structured grid in ANSYS ICEM CFD.

7.2.1 Draft Tube

The draft tube is meshed using the blocking function in ICEM. To maintain a high mesh quality in the circular cross sections, an O-grid is used. Figure 7.6 shows the O-grid at the inlet and outlet. The blocking function ensures an equal amount of nodes in the cross section along the draft tube.

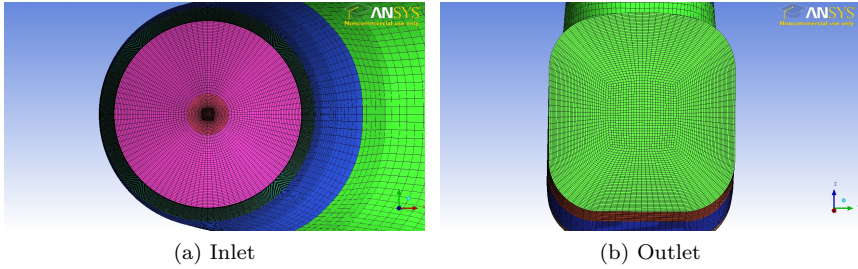


Figure 7.6: O-grid through the draft tube.

Figure 7.7 shows the entire draft tube mesh. The mesh is dense at the inlet and cone, and the density decreases along the flow direction of the draft tube. Because this master thesis is focusing on the flow behavior right after the runner outlet, the mesh density near the draft tube outlet is not a priority.

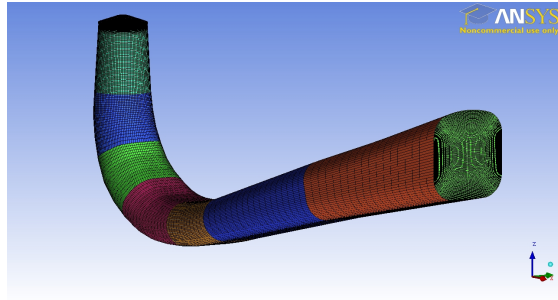


Figure 7.7: Total draft tube mesh.

7.2.2 Runner

The runner is also meshed with the blocking function in ICEM. The geometry of the runner is more difficult than that of the draft tube, which means the meshing is more time consuming. Figure 7.9 the step by step procedure used to mesh the runner. The starting point is the main curves of the runner. A block is inserted, surrounding the runner geometry. The block corners are called vertices, and the block lines are called edges. The block is split into several connected blocks, and the vertices are associated with the appropriate geometry point. After the vertices are associated with the correct geometrical points, the edges are associated with the geometry curves. The amount of nodes on each edge is defined, and the end result of the blocking process is a structure of blocks with predetermined geometrical associations and a defined amount of nodes. The resulting mesh created with the blocking process is shown in figure 7.8.

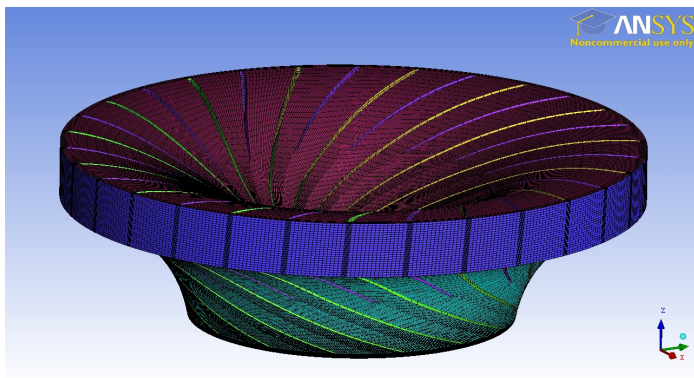


Figure 7.8: The final runner mesh.

7.2.3 Grid sensitivity analysis

To evaluate the grid sensitivity, several meshes are created with an increasing number of nodes for both the runner and the draft tube. Due to limitations in computer memory, a limit of combined nodes is set at 1,500,000 nodes.

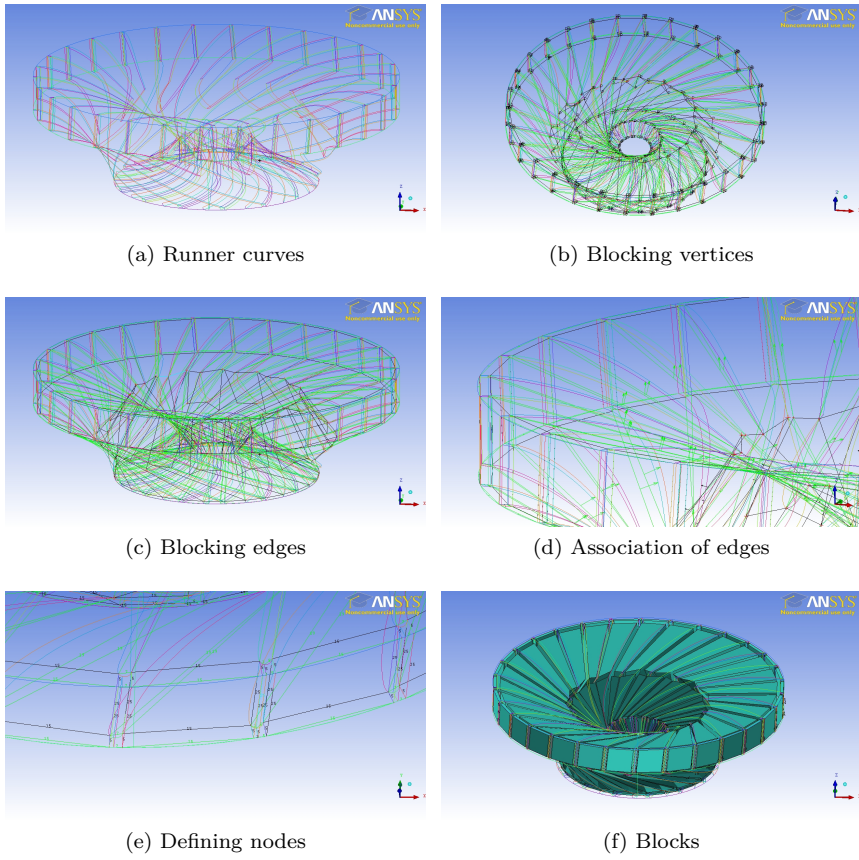


Figure 7.9: The meshing process for the runner.

7.3 Pre-processing

The two meshes are assembled in CFXPre, as the runner domain and the draft tube domain. The assembled Francis turbine is shown in figure 7.10.

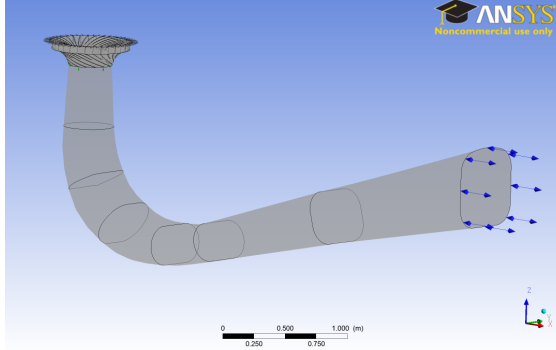


Figure 7.10: Runner and draft tube assembly in CFXPre.

Three operating points are evaluated, the BEP, full load and part load. The operating conditions for the simulations are taken from the Hill chart created by the model test of the turbine. Each operating point has a specific guide vane opening angle, flow factor, and speed factor. From these values, the boundary conditions for the simulations are calculated. Table 7.1 shows the operating conditions for the three operating points.

Table 7.1: Operating conditions from the Hill chart.

Variable	BEP	Full load	Part load
Guide vane opening (α)	10	11	7
Flow factor (Q_{ed})	0,152	0,175	0,093
Speed factor (n_{ed})	0,18	0,165	0,205

7.3.1 Boundary conditions

Runner

The runner domain, shown in figure 7.11 is to rotate about the z-axis. The speed of rotation is defined by the operating point being simulated. Equations (7.1) and (7.2) show the relation between n_{ed} and the turbine rpm in the simulations.

$$n [rps] = \frac{n_{ed} \cdot \sqrt{gH}}{D_2} \quad (7.1)$$

$$[rpm] = n \cdot 60 \quad (7.2)$$

Table 7.2 shows the rpm values for the three operating points in the simulations. As the model runner rotates in the clockwise direction when seen from above, the rpm value in CFXPre must be set as negative.

Table 7.2: RPM values for the operating points in CFXPre.

	BEP	Full load	Part load
RPM	-306	-280	-349

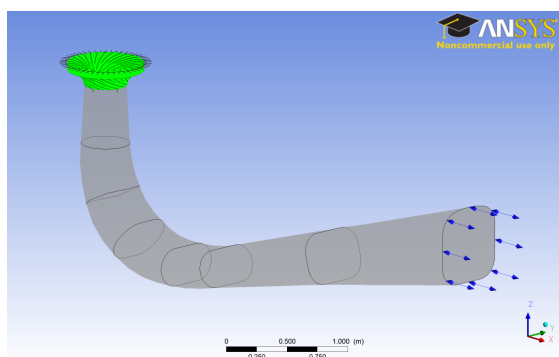


Figure 7.11: Rotating domain in CFXPre.

The hub, shroud, and blades of the runner are set as smooth walls. Because they are part of the rotating domain, they will automatically rotate at the same rpm as the domain. Figure 7.12 shows the walls of the runner.

Figure 7.13 shows the runner inlet. The inlet boundary conditions depend on the operating point. Equations (7.3) shows the relation between Q_{ed} and the mass flow in the simulations. Table 7.3 shows the mass flows for the three operating points in CFXPre.

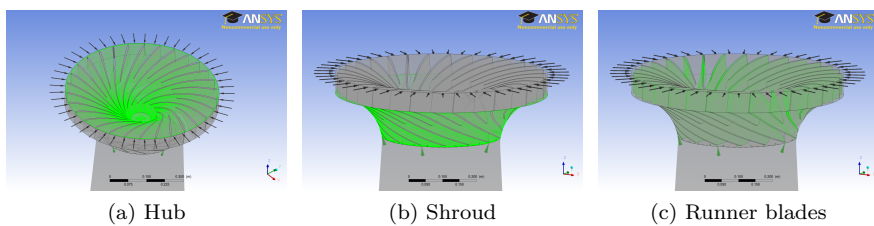


Figure 7.12: Smooth wall boundaries of the runner in CFXPre.

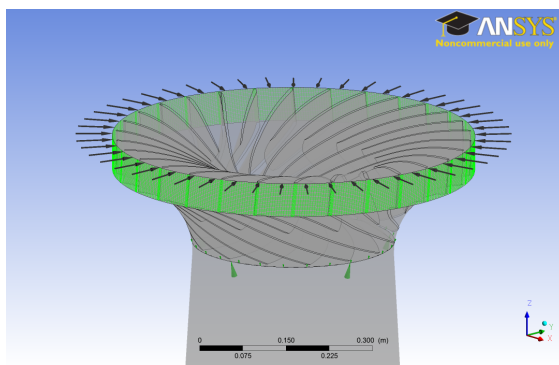


Figure 7.13: Inlet boundary in CFXPre.

$$\dot{m} = Q\rho = Q_{ed}D_2^2\sqrt{gH}\rho \quad (7.3)$$

Table 7.3: Mass flow values for the operating points in CFXPre.

	BEP	Full load	Part load
Mass flow	183	211	112

In order to account for the guide vane opening angle, the flow direction at the inlet is set in cylindrical coordinates. The axial velocity component is assumed to be zero. The tangential velocity component is set as -1 for all the simulations, and the radial component is altered to change the inlet angle. The radial velocity

component for each operating point is calculated using equation (7.4). Table 7.4 shows the velocity components for the simulations.

$$\vec{V}_r = \vec{V}_\theta \tan \alpha \quad (7.4)$$

Table 7.4: Inlet velocity components for the operating points in CFXPre.

	BEP	Full load	Part load
Axial	0	0	0
Tangential	-1	-1	-1
Radial	-0,176326	-0,19438	-0,122784

Draft tube

The draft tube domain, shown in figure 7.14, is set as stationary. The walls of the draft tube are set as smooth walls, and the outlet is set as an opening with -75kPa as the outlet pressure. The draft tube outlet is shown in figure 7.15.

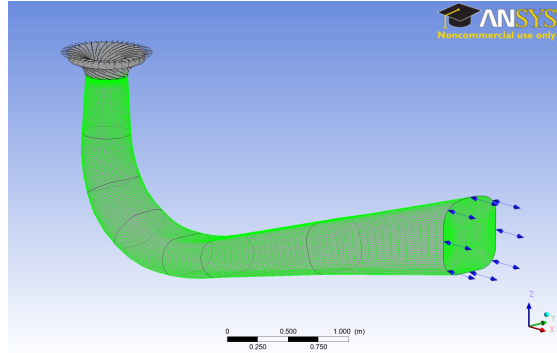


Figure 7.14: Stationary domain in CFXPre.

Runner-Draft tube interface

The interface between the runner and the draft tube, shown in figure 7.16, is a critical part of the simulation. The interface consists of the runner outlet on

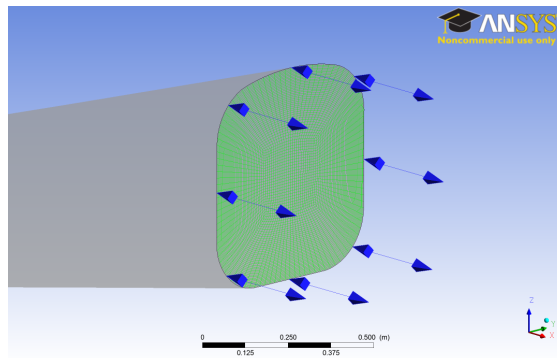


Figure 7.15: Outlet boundary in CFXPre.

one side, and the draft tube inlet on the other side. The connection is a general connection with a frozen rotor. In order to get the effects of the runner rotation in the draft tube flow, the pitch change is set to none.

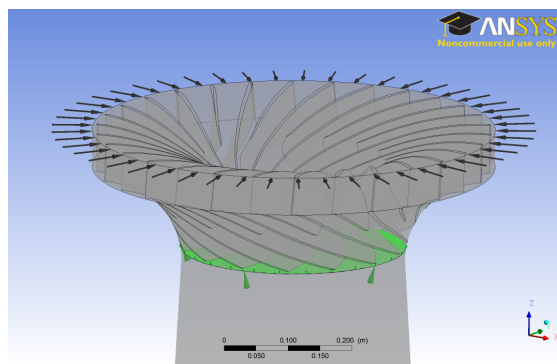


Figure 7.16: Domain interface between runner and draft tube in CFXPre.

7.3.2 Solver definitions

The operating points are evaluated in both steady state- and transient analysis. The two simulation types do not have the same solver setup.

Turbulence

The hybrid turbulence model SST is used in both steady state- and transient simulations. For a description of the SST turbulence model, see appendix A. The turbulence numerics option is set for high resolution.

Advection scheme

The steady state simulations use a high resolution advection scheme, while the transient simulations use the upwind advection scheme.

Convergence criteria

The convergence criteria for the steady state simulations is set at 10^{-4} for the MAX residuals, while the transient simulations are set at 10^{-4} for the RMS residuals. In case there are convergence problems due to the unstable nature of the draft tube flow, the pressure difference from inlet to outlet is monitored. If the residuals do not converge, but the pressure difference stabilizes, the general behavior of the draft tube can still be analyzed.

Transient time treatment

The timestep in the transient analysis is 0,01 seconds. This is a very large timestep considering the short distance between nodes in the mesh and the high velocities. A sufficiently small timestep can be calculated using the stability criterium in equation (7.5)

$$C = \frac{u\Delta t}{\Delta x} \Rightarrow \Delta t = \frac{C \cdot x}{u} \quad (7.5)$$

The analysis is only stable for values of $C < |1|$ [10]. The solver uses the Second Order Backward Euler scheme in time.

7.4 Simulation

A total of nine simulations are performed, three simulations for each operating point. Table shows the simulations performed.

Table 7.5: Simulations performed in CFX.

Sim.	Operation	Type	Δt [s]	Total time	Initial time
1	BEP	Steady state	n/a	n/a	n/a
2	BEP	Transient	0,01	3 s	0 s
3	BEP	Transient	0,01	1 s	3 s
4	Full load	Steady state	n/a	n/a	n/a
5	Full load	Transient	0,01	3 s	0 s
6	Full load	Transient	0,01	1 s	3 s
7	Part load	Steady state	n/a	n/a	n/a
8	Part load	Transient	0,01	3 s	0 s
9	Part load	Transient	0,01	1 s	3 s

The 3 second transient simulations start with no flow in the draft tube, to allow the natural flow of the operating point to develop. The 1 second transient simulations continues from 3 to 4 seconds, with a finer output of results. The 3 second transient analysis creates a results file every 25 timesteps, while the 1 second analysis creates a results file for every timestep. The results from 3 to 4 seconds are used for the final analysis of the draft tube flow at the operating points.

7.5 Post-processing

The post-processing focuses on examining the flow in the draft tube. By specifying locations in the draft tube, CFX can calculate the variables of interest at these locations.

7.5.1 Surfaces

For flow visualization, a cross section of the entire draft tube is created. Figure 7.17 shows the draft tube cross section. This plane is the location for pressure and velocity contours, as well as velocity vectors to examine backflow.

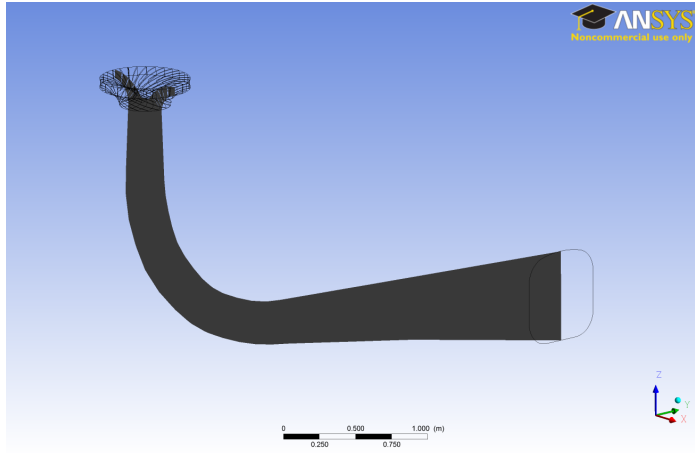


Figure 7.17: Cross section of the draft tube in the ZX plane at $Y=0$.

To examine numerical results, cross sections normal to the flow direction are created through the draft tube. The cross sections are shown in figure 7.18. These cross sections also function as locations for velocity and pressure contours, and velocity vectors. There are 9 cross sections through the draft tube. The first cross section is located at the runner outlet. The second cross section is located 25 cm below the runner outlet in the draft tube cone. The draft tube outlet is the last cross section. The steady state simulations, as well as the 3 second transient simulations, calculate numerical values at all the cross sections. This is in order to ensure the flow is developed fully before the final 1 second transient simulations start. The 1 second simulations focuses on the cross section in the draft tube cone, shown in figure 7.19. This is located 25 cm below the runner, and is also a normal location for pressure measurements in model tests.

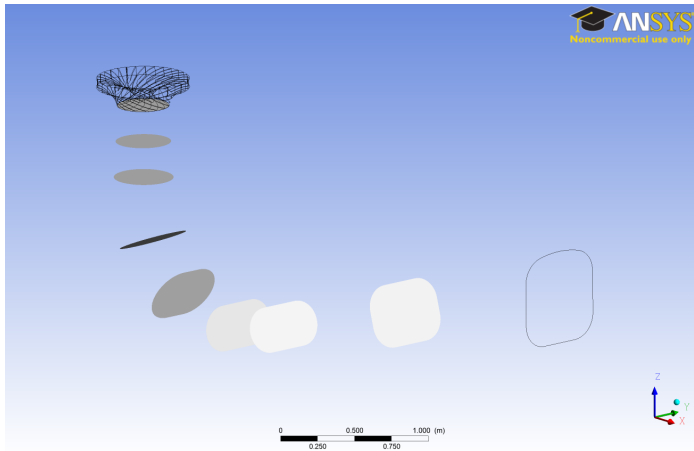


Figure 7.18: Cross sections through the draft tube.

7.5.2 Walls

At the intersection between the draft tube wall and the cross sections in figure 7.18, polylines are created. The pressure measurements at these polylines examine general pressure pulsations in the draft tube. The polylines are shown in figure 7.20.

7.5.3 Points

A point is placed on each of the polylines in figure 7.20. These points examine asynchronous pressure pulsations in the draft tube, and are the basis for the comparison with pressure measurements in the model test.

7.5.4 Iso-surface

To examine the shape of the vortex rope, an Iso-surface of pressure is created. The pressure level can be adjusted to reveal the general shape of a vortex rope.

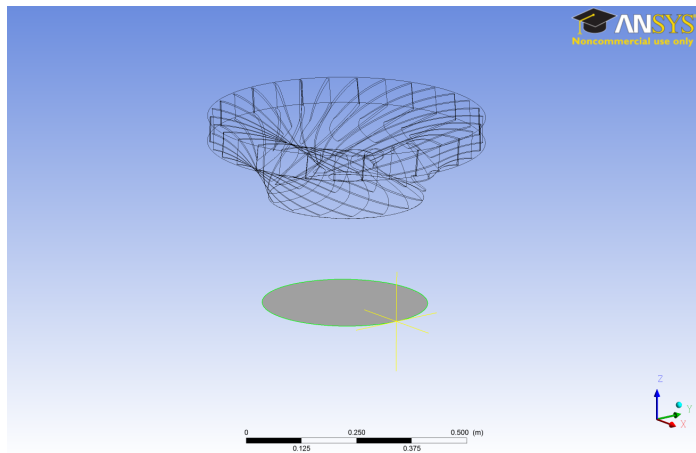


Figure 7.19: Cone cross section.

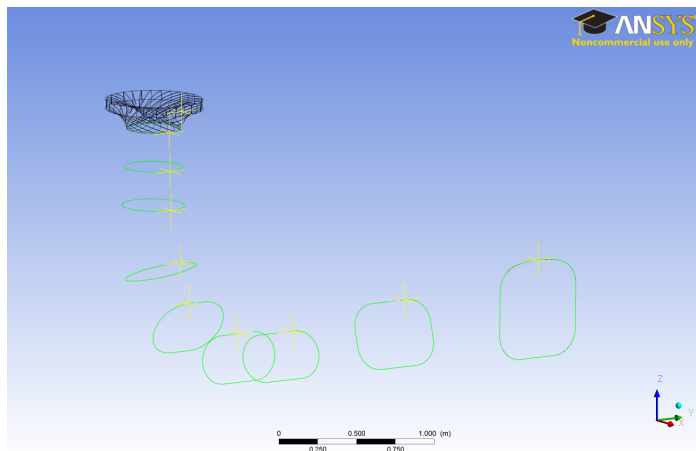


Figure 7.20: Polylines and points on the draft tube wall.

Chapter 8

Experimental Results

8.1 Hill Chart

The results from the model test performed at the beginning of this study suffered from measurement deviations due to calibration errors and defects in some of the measuring instruments. Figure 8.1 shows the hill chart generated from the model test performed by Jørgen Ramdal at the laboratory in 2007.

8.2 Pressure pulsations

There were not performed any pressure measurements in the draft tube cone during this thesis, due to limitations in time and proper equipment. Figure 8.2 shows a FFT of the pressure pulsations measured during the model test performed in 2007 by Jørgen Ramdal at three different operating points.

8.3 Vortex rope

The part load vortex rope is not visible during the model test, however, when altering the pressure in the reservoir tank a vortex rope appears. The vortex ropes at full load and part load are shown in figure 8.3.

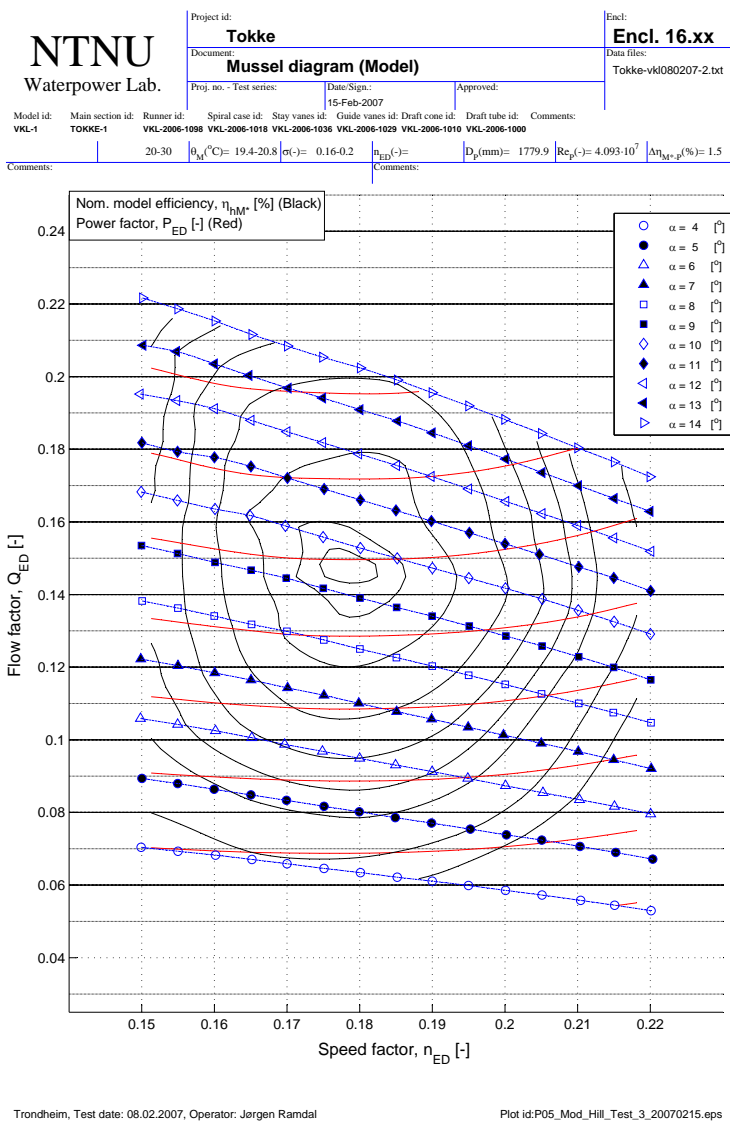


Figure 8.1: Hill chart for the Tokke model turbine.

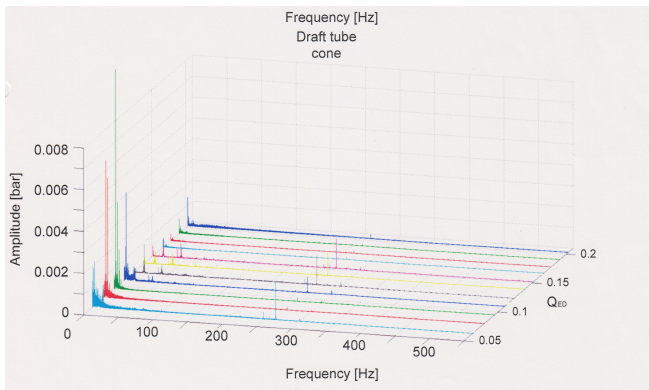
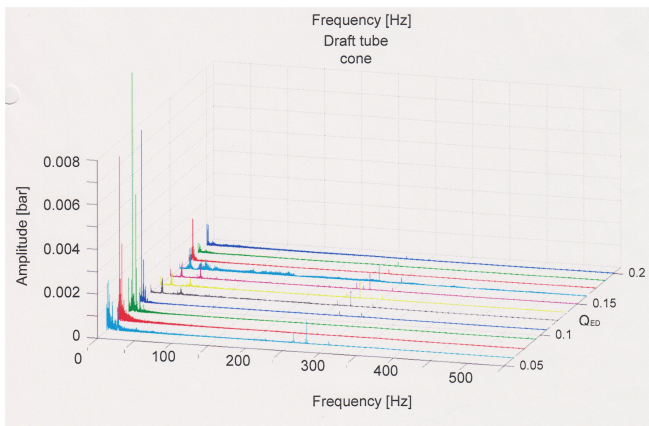
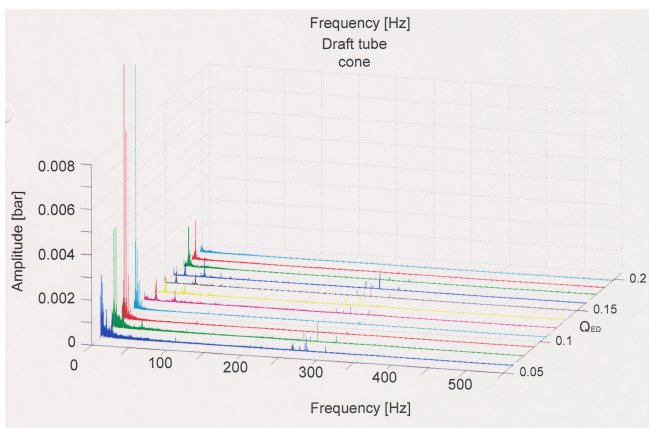
(a) $n_{ed} = 0, 179$ (b) $n_{ed} = 0, 183$ (c) $n_{ed} = 0, 186$

Figure 8.2: FFT of the pressure pulsations measured in 2007.

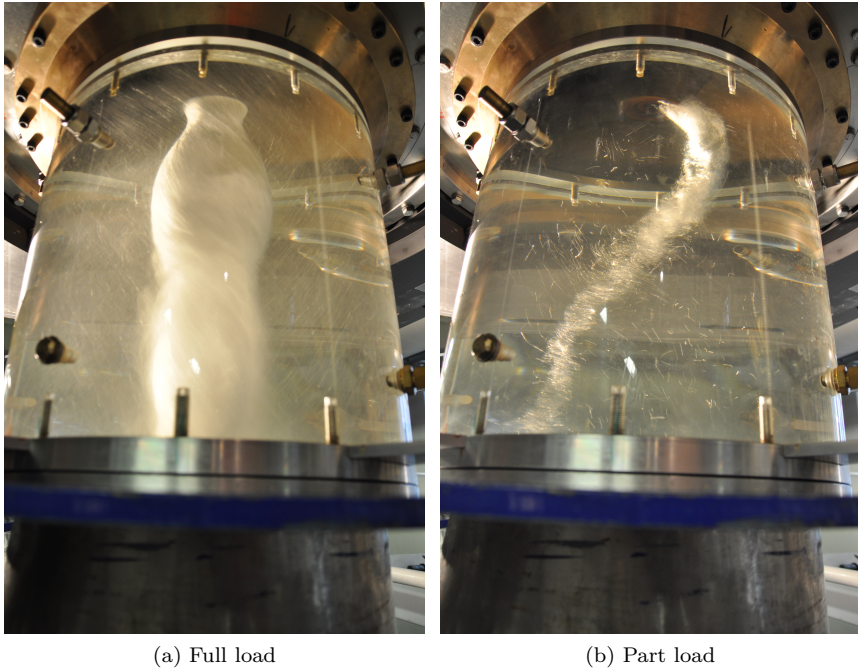


Figure 8.3: Vortex ropes during the model test.

Chapter 9

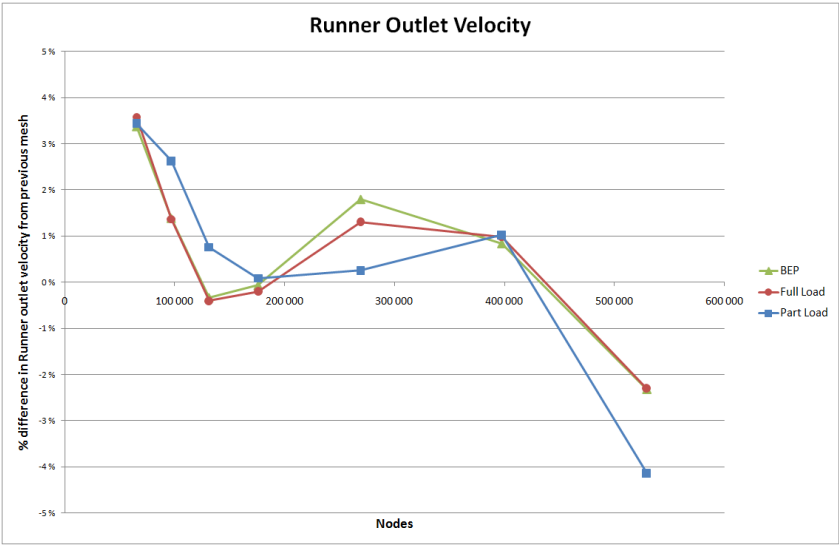
Numerical Results

9.1 Grid Sensitivity Analysis

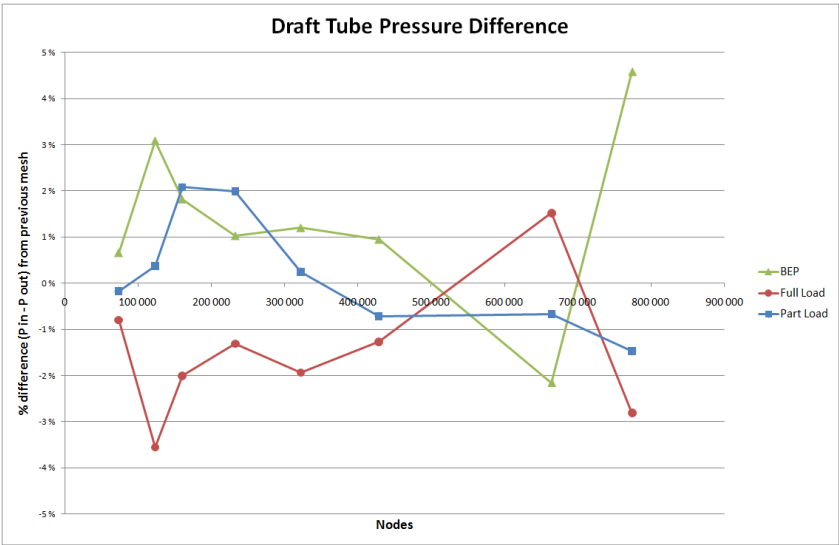
Figure 9.1 shows the grid sensitivity analysis for the runner and the draft tube, respectively. The analysis is inconclusive, as there is no clear indication that the difference in calculated values decrease towards the denser meshes. The meshes used in the simulations have 912.787 nodes for the draft tube, and 642.000 nodes for the runner.

9.2 Steady state simulations

The pressure measurements at the cross sections for the steady state simulations are listed in table 9.1.



(a) Runner



(b) Draft tube

Figure 9.1: Grid sensitivity analysis for the runner and draft tube.

Table 9.1: Pressure measurements from the steady state simulations.

Cross section	Location	BEP	Full load	Part load
Runner outlet	Surface	-76,90 kPa	-80,98 kPa	-76,10 kPa
	Wall	-77,22 kPa	-76,97 kPa	-75,03 kPa
	Point	-77,64 kPa	-77,13 kPa	-75,65 kPa
Cone	Surface	-76,60 kPa	-78,59 kPa	-76,37 kPa
	Wall	-76,04 kPa	-75,88 kPa	-75,64 kPa
	Point	-76,06 kPa	-75,88 kPa	-75,60 kPa
3	Surface	-75,97 kPa	-76,71 kPa	-76,14 kPa
	Wall	-75,78 kPa	-75,68 kPa	-75,72 kPa
	Point	-76,06 kPa	-76,00 kPa	-75,92 kPa
4	Surface	-75,53 kPa	-75,76 kPa	-75,79 kPa
	Wall	-75,44 kPa	-75,32 kPa	-75,44 kPa
	Point	-75,88 kPa	-75,93 kPa	-75,84 kPa
5	Surface	-75,43 kPa	-75,57 kPa	-75,72 kPa
	Wall	-75,32 kPa	-75,24 kPa	-75,52 kPa
	Point	-75,64 kPa	-75,60 kPa	-75,54 kPa
6	Surface	-75,51 kPa	-75,74 kPa	-75,22 kPa
	Wall	-75,49 kPa	-75,57 kPa	-75,21 kPa
	Point	-75,57 kPa	-76,05 kPa	-75,32 kPa
7	Surface	-75,49 kPa	-75,69 kPa	-75,18 kPa
	Wall	-75,49 kPa	-75,55 kPa	-75,18 kPa
	Point	-75,54 kPa	-75,66 kPa	-75,20 kPa
8	Surface	-75,17 kPa	-75,23 kPa	-75,06 kPa
	Wall	-75,17 kPa	-75,23 kPa	-75,06 kPa
	Point	-75,16 kPa	-75,22 kPa	-75,06 kPa
Outlet	Surface	-75,00 kPa	-75,00 kPa	-75,00 kPa
	Wall	-75,00 kPa	-75,00 kPa	-75,00 kPa
	Point	-75,00 kPa	-75,00 kPa	-75,00 kPa

9.3 3 second transient simulations

The pressure is measured at the surface, wall, and point of each cross section. Figures 9.2 and 9.3 show the pressure measured at the points on the cross sections as the flow develops from the initial conditions. The measurements span over 3 second, with a sampling every 0,25 seconds. The development of the wall pressure is shown in figure 9.4, and the surface pressure is shown in figure 9.5.

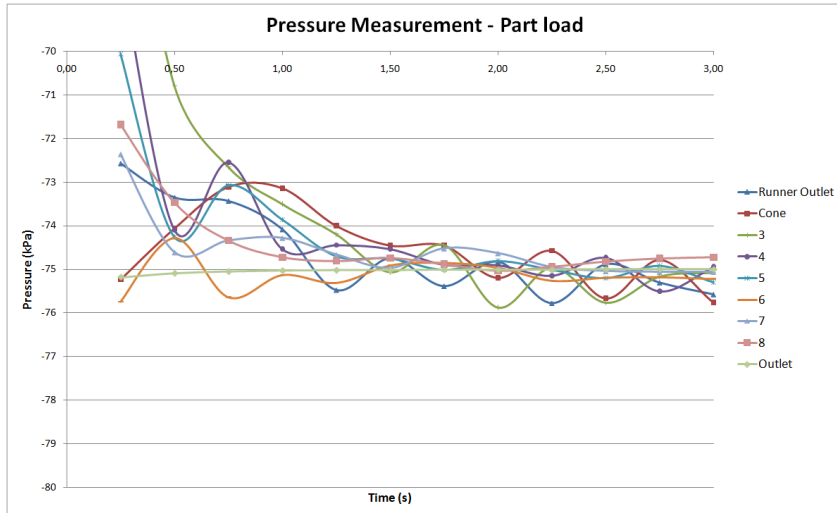


Figure 9.2: Pressure measurements through the draft tube at part load.

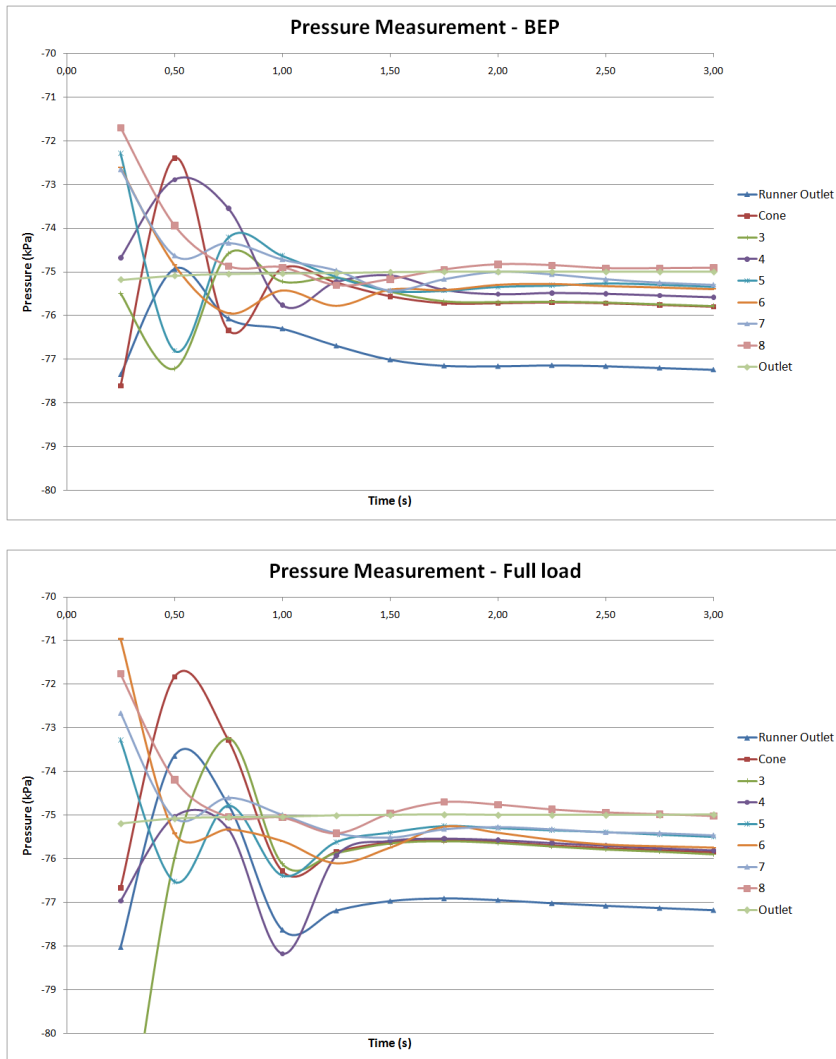


Figure 9.3: Pressure measurements through the draft tube at BEP and full load.

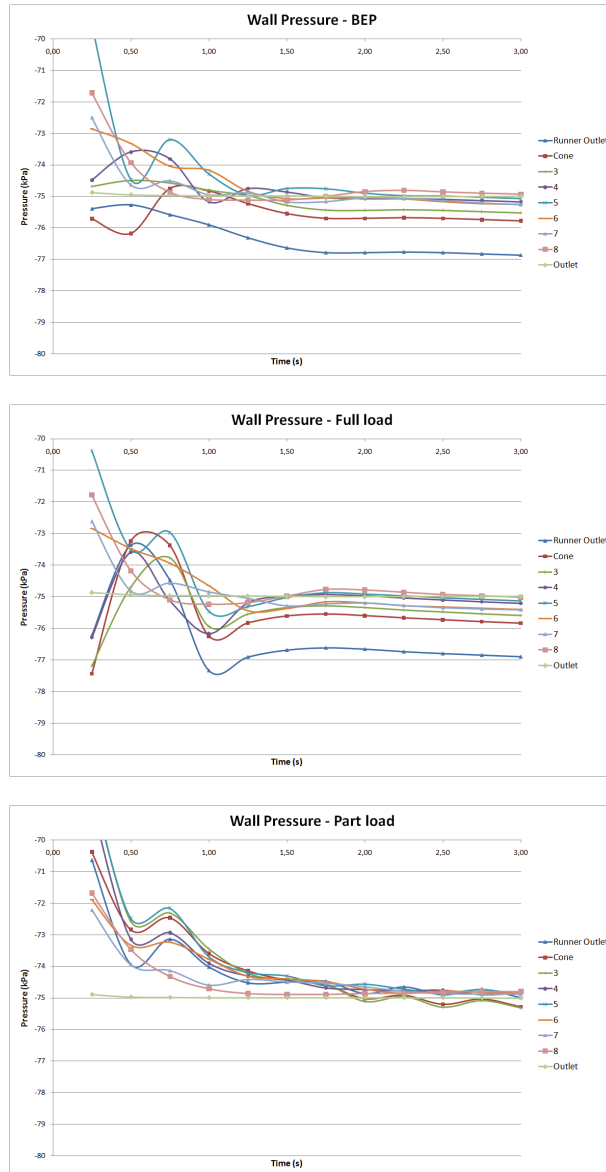


Figure 9.4: Wall pressure through the draft tube.

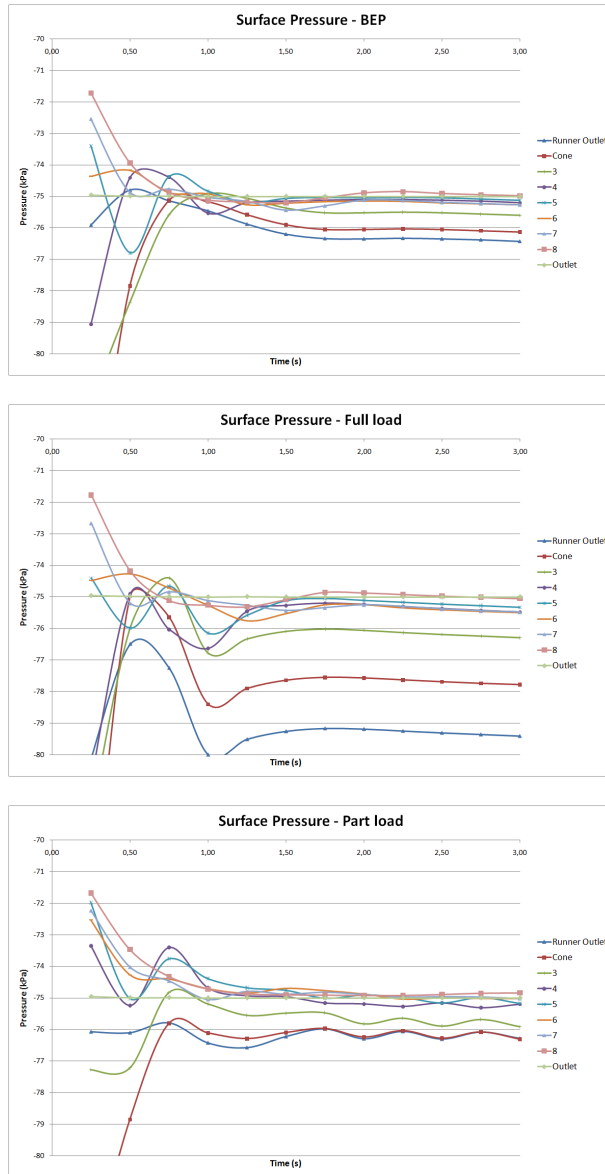


Figure 9.5: Surface pressure through the draft tube.

9.4 1 second transient simulations

Figures 9.6 and 9.7 show the pressure measurements from the cone cross section in the draft tube. The simulation time is from 3 to 4 seconds, with sampling every 0,01 seconds.

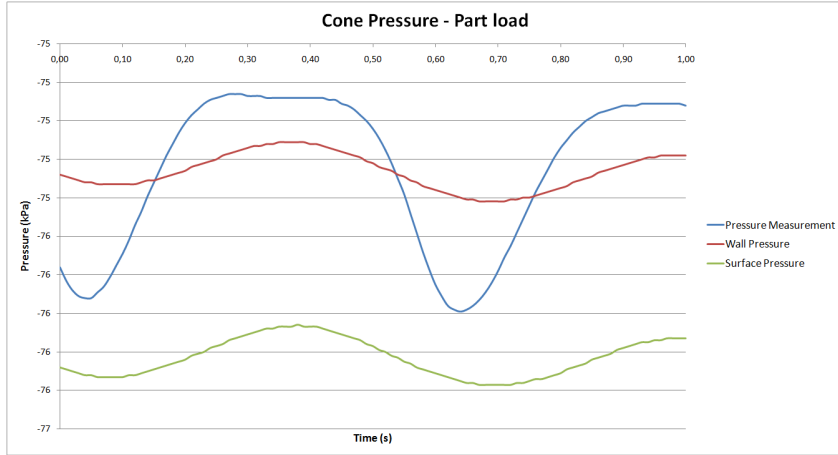


Figure 9.6: Pressure in the draft tube cone at part load.

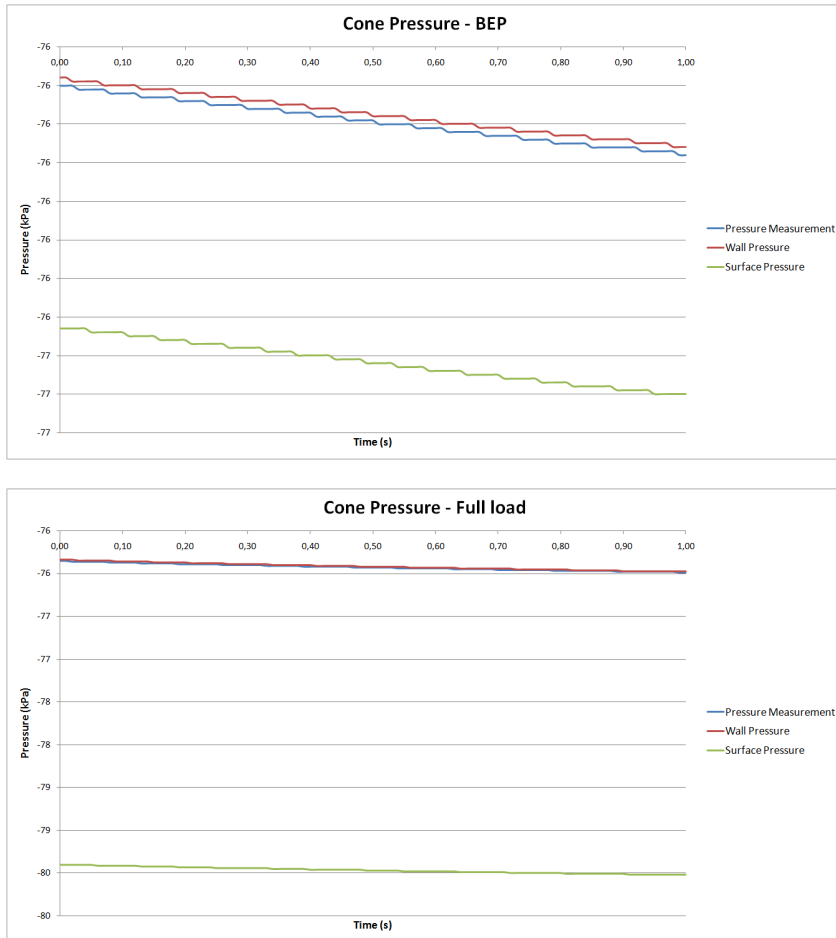


Figure 9.7: Pressure in the draft tube cone at BEP and full load.

9.5 Flow visualization

In order to see the influence the operating point has on the draft tube flow, images from the post-processing are shown for a visual comparison. The results are from the last file of the 1 second transient analysis.

9.5.1 Velocity streamlines

Figure 9.8 shows velocity streamlines through the turbine starting at the runner inlet. The view is close to the runner and draft tube cone, to emphasize the flow difference at the runner outlet between the operating points. The figure clearly shows the difference in flow rotation at the runner outlet.

9.5.2 Draft tube cross section

Figure 9.9 shows the pressure contour on the cross section of the draft tube. The BEP pressure contour shows a small symmetrical zone of low pressure at the tip of the runner hub. When operating at full load, the pressure contour shows a much larger symmetrical zone of low pressure. In the part load operating point, the low pressure zone below the runner hub has become asymmetrical. This is treated in the discussion.

Figure 9.10 shows the velocity contour on the draft tube cross section. Again, the BEP and full load simulations show a symmetric profile, with the full load velocity being greater at the center of the runner axis. The part load simulation shows an asymmetrical velocity compared to the BEP and full load simulations. Figure 9.11 shows velocity vectors on the draft tube cross section. The BEP and full load simulations both give the same visual impression as the velocity contour in figure 9.10. The part load simulation clearly shows backflow, which is treated in the discussion.

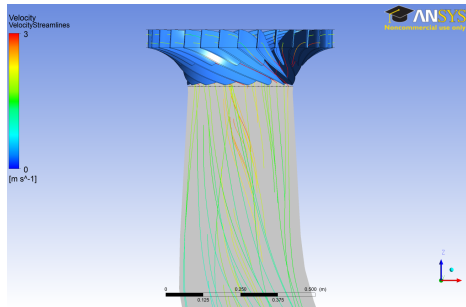
9.5.3 Cone cross section

Figure 9.12 shows the pressure contour, velocity contour, and the velocity vectors at the cross section of the cone. The radial distribution of velocity and pressure indicate stable flows for both the BEP and the full load simulations. Note the opposite direction of the velocity vectors for full load and part load. The asymmetric properties of the part load simulations are treated in the discussion.

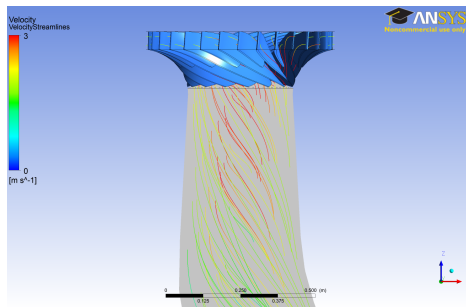
9.5.4 Pressure Iso-surface

Figure 9.13 shows an Iso-surface of pressure at -77 kPa in the draft tube. The figure gives the same impression as the pressure contour. The BEP and full load

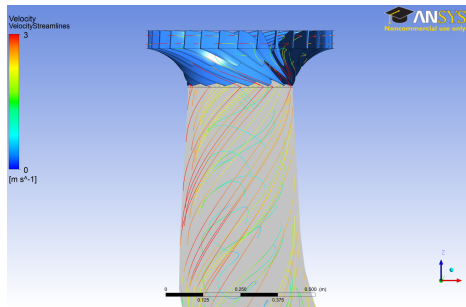
operating points have respectively a small and large symmetrical surface, while the part load surface has a cork-screw shape.



(a) BEP

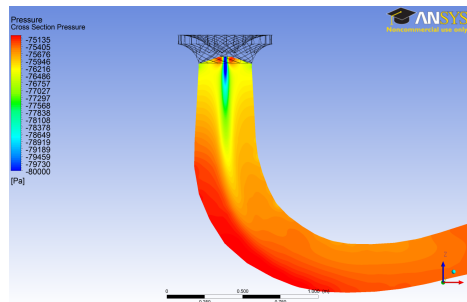


(b) Full load

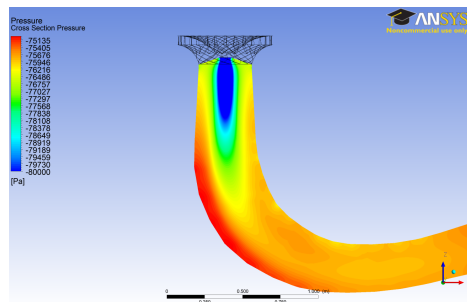


(c) Part load

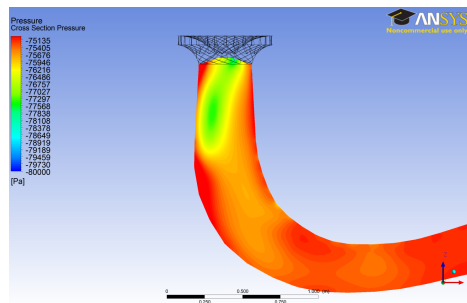
Figure 9.8: Velocity streamlines leaving the runner.



(a) BEP

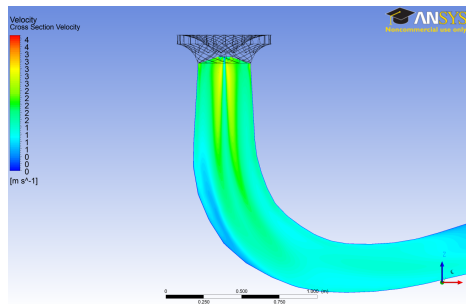


(b) Full load

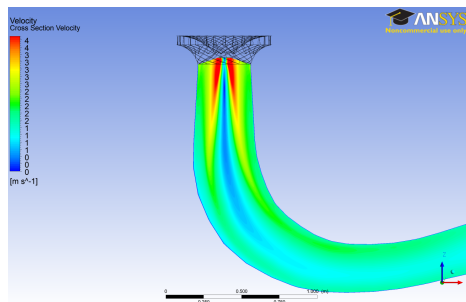


(c) Part load

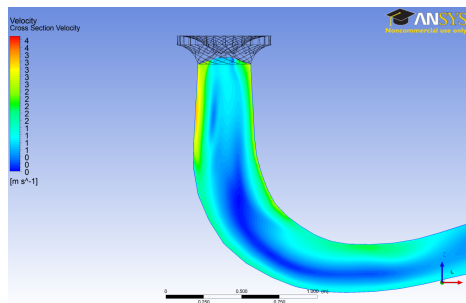
Figure 9.9: Pressure contour at the cross section of the draft tube.



(a) BEP

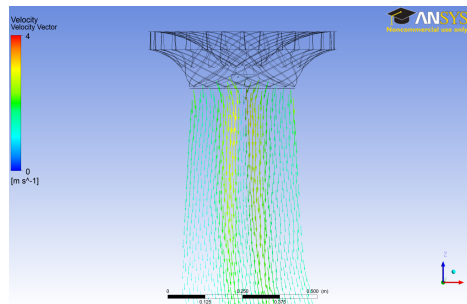


(b) Full load

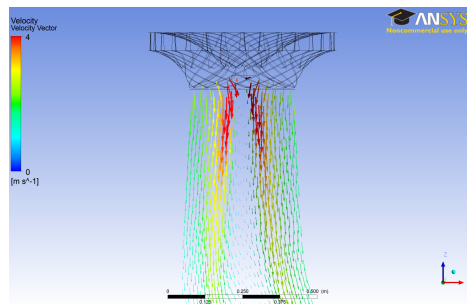


(c) Part load

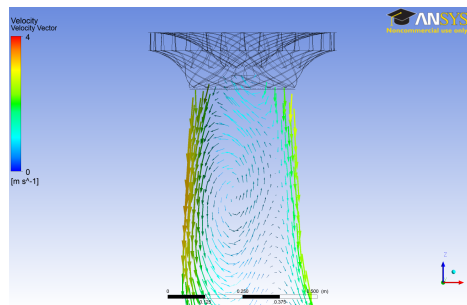
Figure 9.10: Velocity contour at the cross section of the draft tube.



(a) BEP



(b) Full load



(c) Part load

Figure 9.11: Velocity vectors at the cross section of the draft tube.

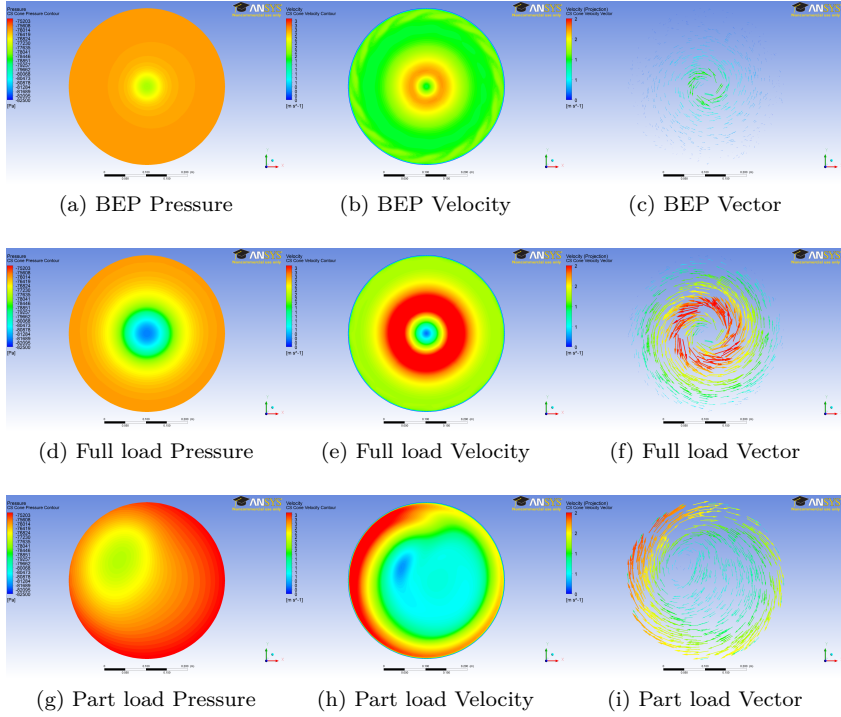
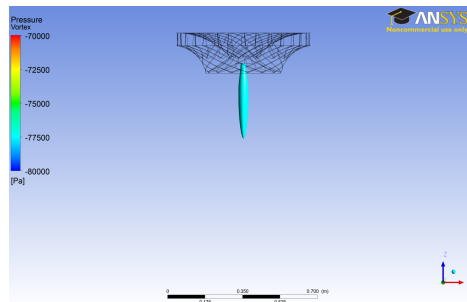
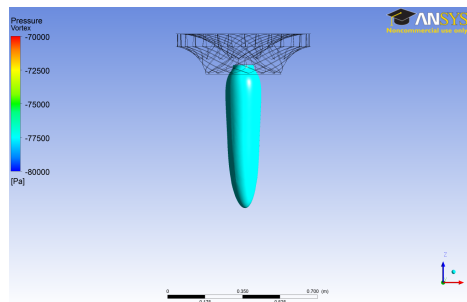


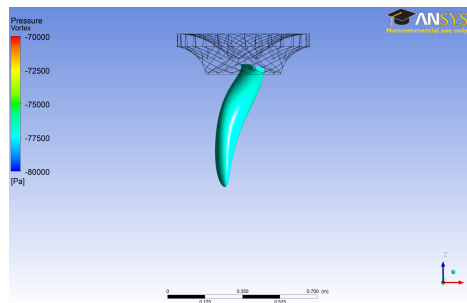
Figure 9.12: Pressure, Velocity, and Vectors in the cone cross section.



(a) BEP



(b) Full load



(c) Part load

Figure 9.13: Pressure Iso-surface at -77 kPa in the draft tube.

Chapter 10

Discussion

Because the BEP and full load simulations resulted in stable and uniform draft tube flows, the discussion will focus on the draft tube flow at part load.

10.1 Flow development

The simulations show a decrease in pressure over time at the draft tube cone. Figure 10.1 shows a comparison between the pressure measured at the draft tube cone in the steady state analysis, and the transient analysis. Although the transient pressure measurements fluctuate about the steady state pressure, the bottom peaks show a decrease in pressure for every period. The flow is therefore most likely not fully stabilized.

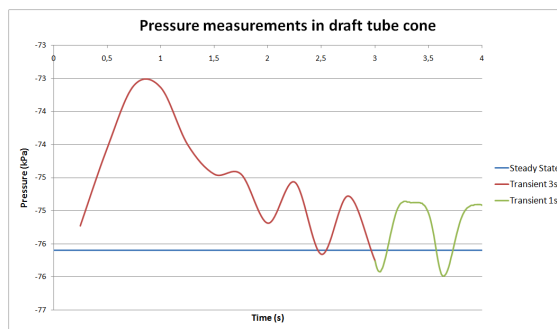


Figure 10.1: Pressure measurements in the draft tube cone at part load.

10.2 Pressure pulsation frequency

The pressure pulsation at the draft tube cone is shown in figure 10.2. The period is measured from the bottom peaks, as they are clearly defined.

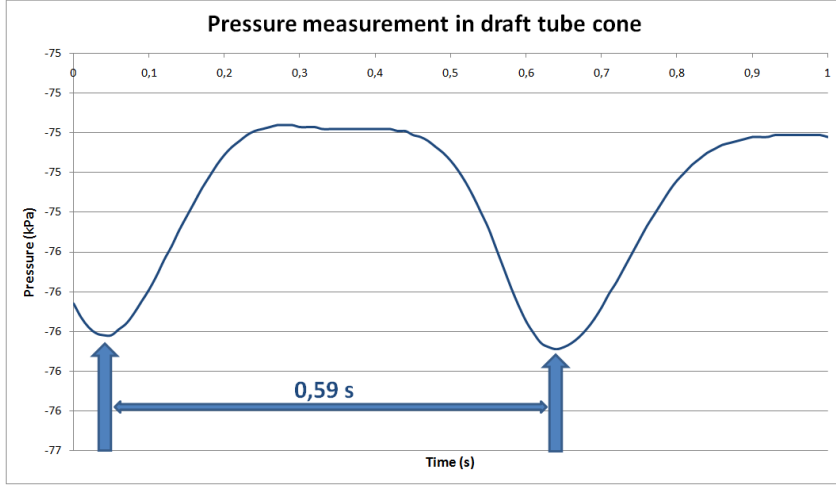


Figure 10.2: Period of pressure pulsation.

With a period of 0,59 seconds, the frequency of the pressure pulsations is calculated as:

$$\text{frequency} = \frac{1}{T} = \frac{1}{0,59} = 1,694915 \approx 1,7$$

10.3 Flow conditions during one period

The pressure pulsation in the 1 second transient analysis, has a rounded top peak compared to the bottom peak. The cause of this is examined by evaluating the flow conditions through the period, to look for natural causes. Figures ?? shows the pressure conditions in the draft tube cone cross section through one period. The pressure is measured at a point, which is visible as a black dot at the right of the cross section. From the figure, it is clear that the low pressure zone in contact with the draft tube wall is smaller than the opposite high pressure zone. This explains the difference in pressure peaks.

10.4 Comparison with model tests

Figures 10.4 and 10.5 show the vortex ropes from the model test and CFD analysis, respectively. The model test vortex rope has a higher angle than the vortex rope from the CFD-analysis.

10.5 Comparison with theoretical frequency

The theoretical definition of the pressure fluctuating frequency, defined in equation (4.8) is:

$$f = \frac{n}{c}$$

with n being the runner speed in rotations per second and c being a number between 3,2 and 4. By rearranging the equation, the frequency from the simulations can be compared.

$$c = \frac{n}{f} = \frac{5,816}{1,7} = 0,29$$

The simulation frequency is lower than the theoretical frequency. This could be caused by a number of errors. The vortex rope in the simulation is an ISO-surface of water, which means the draft tube cone contains only water. The velocity, especially the rotating velocity component, c_u , can be changed when passing through the domain interface between the dunner and the draft tube. This would give the draft tube inlet a velocity profile of a runner with slower rotating speed.

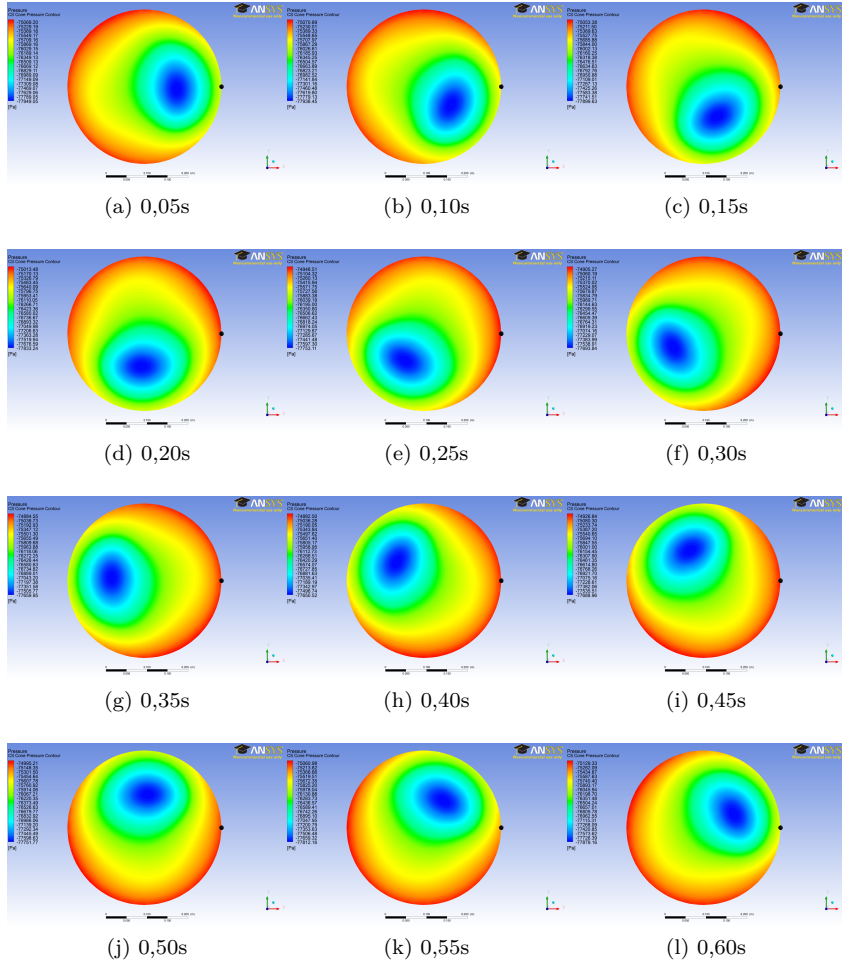


Figure 10.3: Pressure contour in cone cross section at through one period.

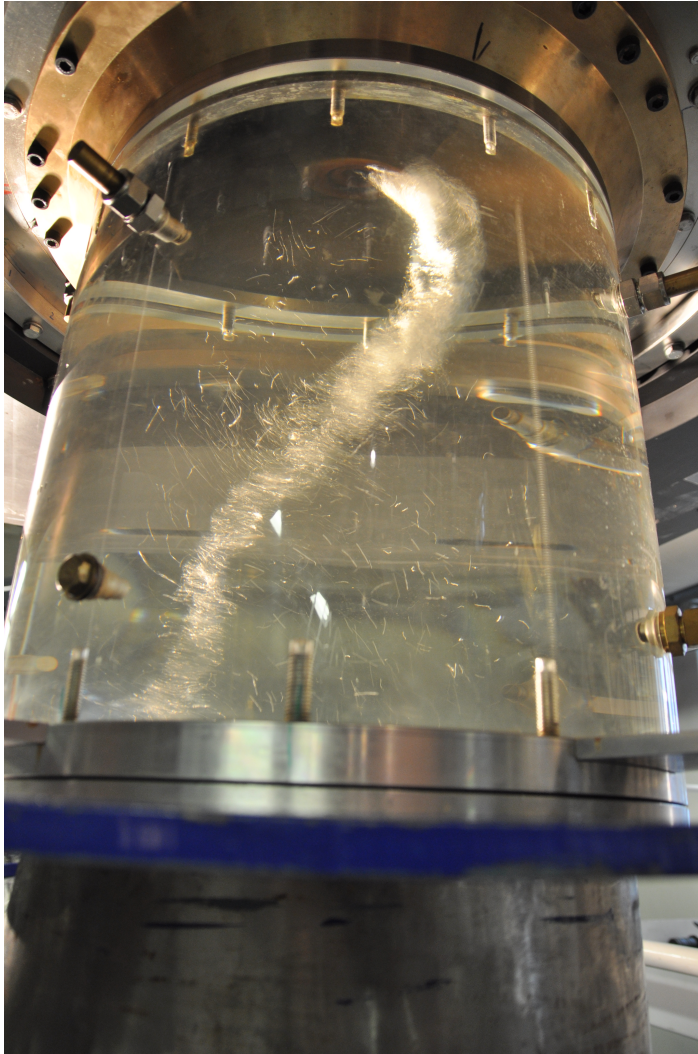


Figure 10.4: Draft tube vortex rope during model test.

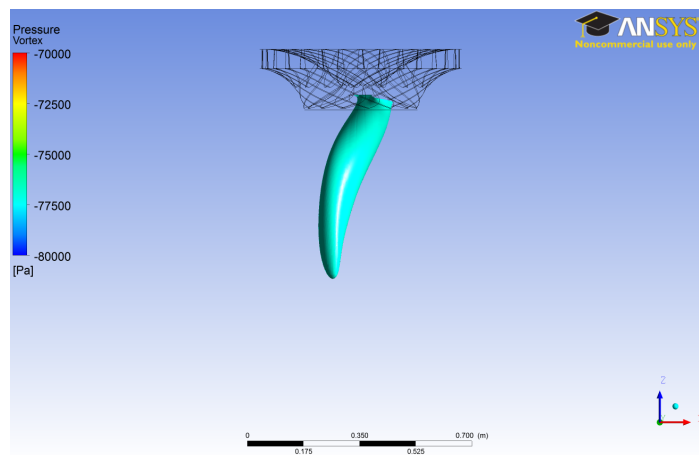


Figure 10.5: Draft tube vortex rope in CFX.

Chapter 11

Conclusion

In this thesis the fluctuating draft tube flow in a Francis turbine operating at part load is investigated. Two types of test are used. A model test of the turbine in the Waterpower laboratory is performed at $H_n = 10m$, and the flow entering the draft tube is analyzed at three operating points, the BEP, full load, and part load. The three operating points are then recreated in a CFD analysis in ANSYS CFX. The primary goal is to perform a transient CFD analysis of the runner and draft tube at part load, and compare the results with experiences from the model test.

The draft tube used in the tests is the Tokke model turbine draft tube in the Waterpower laboratory, and the runner is designed at NTNU.

3D models of the draft tube and runner geometry are created in ANSYS ICEM CFD, and a structured mesh is created for the system. 3 simulations are performed on each operating point, steady state, 3 second transient starting with zero flow in the draft tube, and 1 second transient starting from the last results of the 3 second analysis. The simulation conditions are identical to the model test, with reduced pressure at the draft tube outlet. The CFD solver uses the SST turbulence model, with a high resolution advection scheme and an upwind scheme for the resolution in time.

The simulation results are compared with the model test results and theoretical predictions. Even though the simulations are performed with a single-phase flow, the cork screw shaped draft tube vortex appears at part load. The pulsating frequency of the vortex rope is lower than the theoretical frequency at this operating points, which is most likely caused by numerical dissipation and averaging of the velocity profile from the runner outlet to the draft tube inlet.

Based on the results one can conclude that the CFD simulations at part load produce results that fit with the mathematical models of the draft tube vortex.

The numerical investigations of the turbine enables a more precise evaluation of the flow variables believed to cause draft tube vortex ropes. With increasing computational capacity, this complex flow phenomenon will soon be thoroughly explained.

Chapter 12

Further work

With increased computational capacity, the mesh density can be increased to ensure a grid independent solution. The mesh density near the outlet is not prioritized in this thesis, which can be a source of errors. A denser mesh will also reduce the numerical dissipation of the solutions. Longer transient simulations could examine the pressure drop experienced in this thesis, and verify a fully developed flow. More turbulence models should be examined, to examine possible dissipation reduction in the fluctuating draft tube flow. In order to have a theoretically stable transient solution, the timesteps should be reduced drastically, which would demand an increased computer capacity. In addition, different advection schemes should be examined, which could also contribute to the reduction of the numerical dissipation.

As this thesis focuses on the draft tube flow, the runner performance has not been evaluated numerically. A sufficiently dense runner mesh could evaluate the effects of draft tube surging on the runner performance. This would include a reduction in the Y^+ of the mesh, in order to resolve the boundary layer flow along the walls of the runner. The effect of the runner geometry should also be examined. Hub extensions have been proven to reduce the vortex rope, which is an interesting topic for further numerical investigations.

If the above mentioned problems are solved, it is possible to create an accurate Hill chart with CFD methods only. By simulating the turbine with a two-phase flow, the actual cavitating vortex rope can be examined more thoroughly. In addition, by introducing the spiral casing to the simulations, the impact of the vortex ropes can be investigated to a greater extent.

Bibliography

- [1] H. Brekke, *Pumper og Turbiner*. Vannkraftlaboratoriet NTNU, 2003.
- [2] Y. Hosoi, “Experimental Investigations of Pressure Surge in Draft Tubes of Francis Water Turbines,” *Hitachi Review*, vol. 14, no. 12, 1965.
- [3] M. Fanelli, “On the precession rate of the vortex rope in Francis turbines operation at partial loads,” in *Proceedings of the 10th IAHR International Meeting of the Work Group on The Behaviour of Hydraulic Machinery Under Steady Oscillatory Conditions, Trondheim, June 26-28, 2001*.
- [4] A. Ruprecht, T. Helmrich, T. Aschenbrenner, and T. Scherer, “Simulation of vortex rope in a turbine draft tube,” in *Proceedings of the 21st IAHR Symposium on Hydraulic Machines and Systems, Lausanne, September 9-12, 2002*.
- [5] F. White, “Fluid Mechanics, WCB,” 1999.
- [6] J. J. Cassidy, “Experimental Study and Analysis of Draft Tube Surging,” May 1969. Report No. HYD-591.
- [7] H. T. Falvey, “A Primer on Draft Tube Surging,” *Hydro Review*, pp. 76–86, 1993.
- [8] H. T. Falvey and J. J. Cassidy, “Frequency and amplitude of pressure surges generated by swirling flow,” in *International Association for Hydraulic Research, Hydraulic Machinery Symposium, Stockholm, Sweden, 1970*.
- [9] W. J. Rheingans, “Power Swings in Hydroelectric Power Plants,” in *Transactions of the A.S.M.E.*, 1940.
- [10] H. Versteeg and W. Malalasekera, *An introduction to computational fluid dynamics: the finite volume method*. Prentice Hall, 2007.

- [11] F. Menter, “Two-equation eddy-viscosity turbulence models for engineering applications,” *AIAA journal*, vol. 32, no. 8, pp. 1598–1605, 1994.

Appendix A

ANSYS CFX

A.1 SST Turbulence model

The SST turbulence model combines advantages of both the standard $\kappa - \epsilon$ model and the $\kappa - \omega$ model. The SST model modifies the turbulence production term in the turbulent kinetic energy equation. The production term from the $\kappa - \omega$ model is:

$$P_t = \mu_t \Phi \quad (\text{A.1})$$

The SST model replaces it with:

$$P_t = \min(\mu_t \Phi, C_{lmt} \epsilon) \quad (\text{A.2})$$

By default, the limiting value of C_{lmt} is set to 10^{15} , so equation A.2 is essentially the same as with equation A.1. However, equation A.2 allows the SST model to eliminate the excessive build-up of turbulence in stagnation regions for some flow problems with the use of a moderate value of C_{lmt} . Further, the SST model adds a new dissipation source term in the specific dissipation rate equation:

$$\frac{(1 - F_1) 2\rho\sigma_{\omega 2}}{\omega} \left[\frac{\partial \kappa}{\partial x} \frac{\partial \omega}{\partial x} + \frac{\partial \kappa}{\partial y} \frac{\partial \omega}{\partial y} + \frac{\partial \kappa}{\partial z} \frac{\partial \omega}{\partial z} + \right] \quad (\text{A.3})$$

Here, F_1 is a blending function that is one near the wall surface and zero far away from the wall. The expression of the bending function F_1 is given by Menter [11], and with the help of F_1 , the SST model automatically switches to the $\kappa - \omega$ model in the near wall region and the $\kappa - \epsilon$ model away from the walls. The model coefficients are all calculated as functions of F_1 :

$$\varphi = F_1 \varphi_1 + (1 - F_1) \varphi_2 \quad (\text{A.4})$$

Here, φ stands for the model coefficients σ_κ , σ_ω , β' , and γ of the SST model, and φ_1 and φ_2 stand for the model coefficient of the $\kappa - \omega$ model and the $\kappa - \epsilon$ model respectively. Default values for the various constants in the SST model are given in table A.1

Table A.1: SST model coefficients

Constant	Default value in CFX
C_{lmt}	10^{15}
$\sigma_{\kappa 1}$	1,176
$\sigma_{\omega 1}$	2,0
γ_1	0,5532
β'_1	0,075
$\sigma_{\kappa 2}$	1,0
$\sigma_{\omega 2}$	1,168
γ_2	0,4403
β'_2	0,0828